NORTHWESTERN UNIVERSITY

Bio-informed Image-based Deep Learning Frameworks for Prognosis of Pediatric Spinal Deformities

A DISSERTATION

SUBMITTED TO THE GRADUATE SCHOOL
IN PARTIAL FULFILLMENT OF THE REQUIREMENTS

for the degree

DOCTOR OF PHILOSOPHY

Mechanical Engineering

By

Mahsa Tajdari

EVANSTON, ILLINOIS

March 2022

ABSTRACT

Bio-informed Image-based Deep Learning Frameworks for Prognosis of Pediatric Spinal Deformities

Mahsa Tajdari

Predicting pediatric spinal deformity (PSD) from X-ray images collected on the patient's initial visit is a challenging task. This research provides a bio-informed framework based on a mechanistic machine learning technique with dynamic patient-specific (PS) parameters to predict PSD. We provide a geometry-based bone growth model that can be utilized in a range of applications to enhance the bio-informed mechanistic machine learning framework, taking dynamic aspects into account. The proposed technique is being utilized to examine and predict spine curvature in PSD cases such as adolescent idiopathic scoliosis (AIS). The best fit of a segmented $3D$ volumetric geometry of the human spine acquired from $2D$ X-ray images is employed. Using an active contour model based on gradient vector flow (GVF) snakes, the anteroposterior and lateral views of the X-ray images are segmented to derive the $2D$ contours surrounding each vertebra. The snake parameters are calibrated on the

dataset, resulting in considerable improvement in image segmentation and data collection. The $2D$ segmented outlines of each vertebra are transformed into a $3D$ image segmentation result. The Iterative Closest Point (ICP) mesh registration technique is then used to establish a mesh morphing approach and creates a $3D$ Atlas spine model. Using the comprehensive $3D$ volumetric model, one can automatically extract spinal geometry data as inputs to the mechanistic machine learning network. The proposed bio-informed deep learning network with the modified bone growth model not only significantly outperforms other state-of-the-art model-based methods, but also achieves competitive or even superior performance against state-of-the-art learning-based methods.

Acknowledgements

I would like to express my sincerest appreciation to my dissertation advisor, Professor Wing Kam Liu, for all his guidance, support, and most importantly, care and patience throughout my Ph.D. study at Northwestern University. Professor Liu has always encouraged me to be an independent researcher with confidence. His breadth of knowledge, creativity and infectious enthusiasm have always made working with him a pleasure. Without his guidance and persistent help, this dissertation would not have been possible.

I want to express my deepest gratitude to Professor Jessica Zhang, for her valuable comments and for providing helpful resources through my course of study. She is a phenomenal professor and an exceptional role model who always supported me throughout my Ph.D. research. I am eternally grateful to Professor Gregory Wagner for his valuable insights and helpful feedback over the years. Professor Wagner is an excellent source of inspiration, and I am deeply appreciative of all his support and advice.

I want to express my most profound acknowledgment to Professor John Sarwark for providing excellent clinical support for this research. He also gave valuable suggestions and skillful reflection concerning these projects. I also want to thank Professors Mark Fleming for teaching me and inspiring my thinking.

I would like to acknowledge my colleagues from other research institutes: Farzam Tajdari and Dr. Aishwarya Pawar, for working with me on the imaging part, Dr. Ayesha Maqsood for her help on the clinical side, Pouyan Shirzadian for his help and endeavor through all steps of my research and Dr. Mirwais Wardak for his support and helpful insights.

Graduate school has been one of the best times of my life. Part of the reason for this is that I had an incredible group of colleagues to work with. I would like to extend my deepest thanks to all the current and former members of Prof. Liu's Lab: Dr. Jyaing Gao, Dr. Ye Lu, Dr. Jiapeng Liu, Dr. Puikei Cheng, Dr. Kevontrez Jones, Sourav Saha, Hengyang Li, Chanwook park, Satyajit Mojumder, and Xiaoyu Xie.

Having a lovely family that has always been there for me with their love, support, and sense of humor has always been a huge source of happiness. Masoumeh and Mehdi, my parents, have given me every chance to pursue my goals. They have always been my strongest supporters, and I am eternally thankful for all they have done for me. I will never be able to repay them for all they have done for me, but I will start by dedicating my dissertation to them. I would also want to express my gratitude to Mahdis, my lovely sister, for her patience, thoughtful support, and sage advice during my Ph.D. journey.

Final words of thanks go to God, who has been a constant presence in my life as I have traveled through it. I would not have been able to finish this task without His help.

Preface

This dissertation involves research on pediatric spinal deformity analysis. The following papers serve as the dissertation's foundation and will be properly cited.

(1) Mahsa Tajdari, Farzam Tajdari, Pouyan Shirzadian, Aishwarya Pawar, Sourav Saha, Toon Huysmans, Yu Song, Yongjie Jessica Zhang, John F. Sarwark, and Wing Kam Liu. Next generation prognosis framework for pediatric spinal deformities using bio-informed deep learning networks. Submitted in special issue on "Image-based methods of computational medicines" of Engineering with Computers, submitted Jan 31, 2022.

(2) Mahsa Tajdari, Aishwarya Pawar, Hengyang Li, Farzam Tajdari, Ayesha Maqsood, Emmett Cleary, Sourav Saha, Yongjie Jessica Zhang, John F Sarwark, and Wing Kam Liu. Image-based modelling for adolescent idiopathic scoliosis: Mechanistic machine learning analysis and prediction. Computer methods in applied mechanics and engineering, 374:113590, 2021.

(3) Hengyang Li, Orion L Kafka, Jiaying Gao, Cheng Yu, Yinghao Nie, Lei Zhang, Mahsa Tajdari, Shan Tang, Xu Guo, Gang Li, et al. Clustering discretization methods for generation of material performance databases in machine learning and design optimization. Computational Mechanics, 64(2):281–305, 2019.

(4) Sourav Saha, Zhengtao Gan, Lin Cheng, Jiaying Gao, Orion L Kafka, Xiaoyu Xie, Hengyang Li, Mahsa Tajdari, H Alicia Kim, and Wing Kam Liu. Hierarchical deep learning neural network (hidenn): An artificial intelligence (ai) framework for computational science and engineering. Computer Methods in Applied Mechanics and Engineering, 373:113452, 2021.

Dedication

To my parents and my sister.

Table of Contents

List of Figures

List of Tables

CHAPTER 1

Introduction

1.1. Motivation and objectives

Spine deformities are common pediatric and adolescent conditions and these conditions may lead to health risks ranging from pain, loss of function, to even pulmonary and cardiopulmonary difficulties. If the spine loses its usual, graceful S-shape (when seen from the side), or if the spine loses its straightness, deformities may arise as a result (viewed front to rear). The term Pediatric Spinal Deformity (PSD) refers to malformations of the spine in children, such as scoliosis, kyphosis, and spondylolisthesis [**10**]. Scoliosis and kyphosis are conditions characterized by aberrant curvature of the spine, while spondylolisthesis is characterized by the displacement of vertebrae. PSD is caused by a variety of etiologies; the most common of which is idiopathic scoliosis and importantly occurs during phases of growth and development. Bone growth of the vertebrae is affected directly, leading to progression and advancement of deformity.

Adolescent Idiopathic Scoliosis (AIS) is used to describe one of the most prevalent spinal conditions in children and adolescents. AIS accounts for around 80% of all pediatric scoliosis cases, affecting approximately 3% of adolescents under the age of 16 in the United States [**11**] roughly 7 million individuals in the United States. There remains more to learn about the underlying pathophysiology of PSD.

While the human spine is composed of 24 vertebrae, only 17 are of interest to AIS analysis. Thoracic (T 1-12) and lumbar (L 1-5) vertebrae, shown in Figure 1.1, are assumed to be responsible for scoliosis, making them the focus of diagnosis and treatment. Note that the treatment of scoliosis is mainly reliant on the shape and extent of spinal curvature, and specific treatment choices are usually determined by the surgeon's expertise. As a result, the development of a clinically validated, patient-specific (PS) model of the spine to assist surgeons in identifying early-stage PSD would guide optimum surgical and non-surgical treatment options, resulting in significant therapeutic benefit. For both screening and monitoring in present clinical practice, the lack of an appropriate safe, inexpensive, and accurate measuring technology is a major need in clinical practice. To track the evolution of deformities throughout adolescent growth, frequent imaging is essential [**12**] and the extracted features from medical images such as Cobb angle determine the severity of spinal deformity.

It is common practice in spine surgery to use computer-aided procedures, such as advanced imaging for improved surgical navigation (to determine safe placement or a surgical path for implants [**13, 14, 15**]), for more successful execution of the surgical plan [**16, 17**]. One of the greatest barriers to incorporating these technologies into clinical practice is the time and effort necessary to generate PS functional models from medical imaging. It entails a number of manual procedures and is time intensive, even for seasoned specialists [**18, 19**]. For example, image segmentation is both time-consuming and user-dependent [**20, 21**]. Certain software applications support automated image analysis of the spine. However, it is often required to locate and segment vertebrae ahead of time, which is a time-consuming operation [**22**]. Due

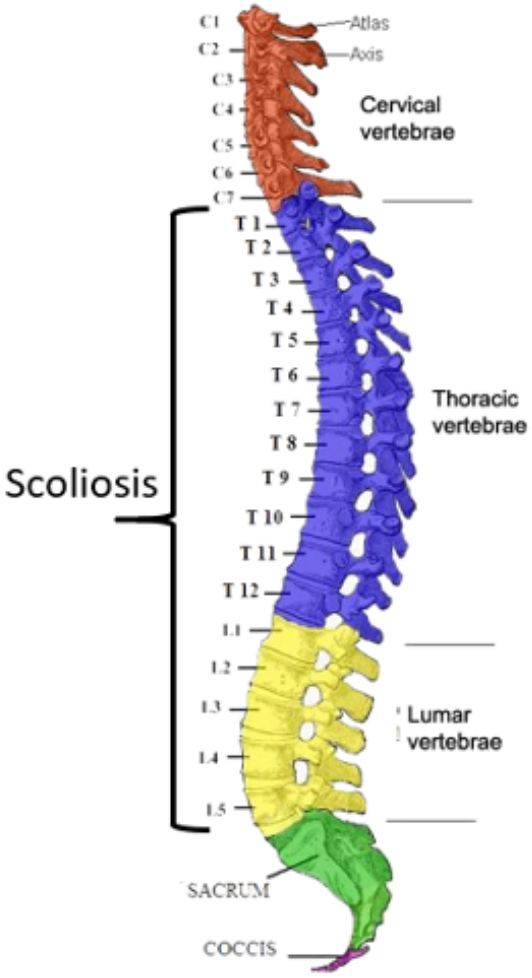

Figure 1.1. Diagram of the the human spine, the thoracic (T1 to T12) and the lumbar regions (L1 to L5) are responsible for scoliosis.

to the 2D nature of the X-ray data, generating 3D detailed geometry of the spine from a 2D set of X-ray images is a challenging task [**23, 24**]. Furthermore, various manual processes are required to segment the obtained volumetric mesh in order to detect hard and soft tissue once the 3D model has been formed. Machine learning (ML) approaches, on the other hand, need a large amount of data to be trained and provide reliable results. The absence of reliable medical data for a given individual

over time is one of the challenges in implementing ML for prognosis spinal deformity. Furthermore, these models are referred to as "data-hungry" approaches since they cannot forecast outside of the range of the training data. Recent publications show that by including physics into the system, one may enhance the model's predictability range [**25**]. However, for spinal curve progression including bone formation, PS governing physical equations with time-varying and geometric-based coefficients are unavailable.

Previously published research in [**2**] used X-ray imaging data to develop a prognostic framework for AIS. This framework predicts spine morphology by combining clinical data acquired from X-ray images with mechanistic features extracted from a spine surrogate model along with the bone growth model. Despite this framework presented a unique technique to using mechanistic data science for forecasting spine deformity, the method has a number of limitations that impede deploying this framework in real-world scenarios. One restriction is the manual parameter adjustment for image segmentation of each vertebra. The presented $3D$ reconstruction and geometry generation technique requires considerable labor since each tissue is generated separately and all tissues are assembled together. Moreover, the bone growth model has constant parameters throughout all patients and time steps. However, these assumptions are unrealistic since bone formation differs across ages and vertebrae. The proposed framework predicts a 2D image of the spine, while AIS is a 3D deformation. The framework is only evaluated for landmarks placed on the growth plate and does not take into account all points derived from X-ray data.

Challenges in analyzing the PSD through modeling can be summarized as:

- Lack of consistent medical data for a specific person over time;
- Need for a swift predictive method suitable to be used by the medical practitioners;
- Time-consuming process of segmenting medical images;
- Generating patient-specific volumetric mesh and extracting required information;
- The absence of knowledge to understand the governing physics of the problem; and
- Combining all information to come up with a predictive model despite having limited data.

This dissertation aims to address the concerns above by developing a bio-informed mechanistic machine learning framework that can predict spinal curvature using the available limited patient-specific data.

1.2. Related works

1.2.1. Vertebrae image segmentation

Precisely segmenting the vertebrae is critical for subsequent analysis in an injury detection system. Statistical shape model (SSM)-based techniques have dominated previous work in vertebral segmentation [**26, 27**]. Based on a training set, these approaches capture statistical information on the shape and/or appearance of the vertebra. The mean shape is then manually or semi-automatically set close to the real vertebra, and a search process is used to converge the shape on the true vertebral boundaries. Latest evidence has used random forest-based machine learning (ML)

models to achieve shape convergence [**28, 27, 29, 30**]. These approaches, however, are only efficient and accurate for the restricted data reported in the literature and cannot be applied to PS datasets.

1.2.2. 3D model development and computational simulation

Compared to MRI and computational tomography (CT) scanners, X-ray images are more commonly employed due to their accessibility, lower cost, shorter scanning time, and lower ionizing radiation levels particularly for adolescent patients. Statistical Shape Models (SSM) [**31, 32, 33, 34**] or Statistical Shape and Intensity Models (SSIM) were used to reconstruct bones from X-ray images. To prevent local maxima while optimizing the deformable model parameters, it is important to select a reasonable starting point [**35, 36**]. Recent years have seen the use of deep learning to recognize landmarks and triangulate them [**35**]. However, performing 3D reconstruction from two or more 2D photos using a deep learning technique remains a tough problem due to the complexity of describing a dimensional expansion in multi-view circumstances. The EOS imaging system (formerly, Biospace Med, Paris, France), the DIERS formetric scanner, and ultrasonography are examples of recent breakthroughs in diagnostic imaging for AIS [**12**]. The EOS imaging system is made up of two orthogonal pairs of X-ray tubes and detector units that allow for the simultaneous capture of anteroposterior (AP) and lateral (LAT) X-ray pictures while standing. EOS imaging can quickly scan the spine in 8–15 seconds, depending on the patient's height. From the EOS anteroposterior and lateral pictures, the software system sterEOS (EOS Imaging, Paris, France) can generate a highly accurate 3D

model of the spine [**37, 38, 39**]. However, this technology is unable to divide distinct tissues in order to account for the many biological organs. Due to its expensive cost, it is not widely available in many medical centers.

To gain a better knowledge of load distribution and other mechanical features, the 3D generated PS geometry may be utilized to construct a finite element model. There is no comprehensive automated workflow for anatomically correct FE simulations of the spine based on 2D X-ray data. A lot of work has been done on parametric FE models or a mix of statistical and FE models [**40, 41**]. However, those models either ignore essential PS features or require a lot of manual labor, which necessitates a certain level of operator experience. Although efforts to automate the construction of FE models of the healthy spine have been performed [**42, 19**], the technique has never been integrated with deep learning-based segmentation algorithms or applied to diseased situations.

1.2.3. Implementing ML for studying spinal deformity

The application of artificial intelligence (AI) in medical research [**43**] has skyrocketed in recent decades. ML is a subset of AI that allows computers to discover patterns from data without explicit programming. These approaches, however, are characterized as data-hungry methods since they always rely on the training data [**44**]. When it comes to medical image analysis, there has always been the challenge of how to accurately integrate ML for disease diagnosis, prognosis, and therapy. A framework with such characteristics should always be able to capture the biological governing equation in order to offer extra information in addition to the training data. Recent

studies have attempted to use AI to predict spinal deformities [**45, 46, 47, 48**]. These frameworks, on the other hand, cannot be applied to other disciplines. Recently, research has shown that by incorporating the system's underlying physical equations, the framework may forecast data outside of the projected range [**2, 49**]. However, there are certain processes in between that need manual parameter adjustment and, as a result, cannot be implemented for real-time prognosis framework.

1.3. Contribution and outline of the dissertation

This dissertation introduces a flexible and powerful bio-informed mechanistic neural network architecture that aims to push the limits of existing methods by calibrating time-varying geometry based parameters for prognosticating 3D shape spinal deformity. Moreover, the framework is enhanced by calibrating image segmentation algorithm variables. To generate detailed geometry, the segmented data is fed into a 3D reconstruction tool. A novel bone growth model is proposed to potentially improve neural network prediction performance without adding additional computational burden, and a thorough analysis of parameter setting, intermediate results, and cross-validation studies is provided to better support the working mechanism of the proposed bio-informed mechanistic deep learning framework. The contribution of this dissertation is summarized as follows:

- Predicting pediatric spinal deformity (PSD) progression using bio-informed mechanistic machine learning;
- Calibrating parameters of image segmentation to expedite the process;
- Generating patient-specific volumetric mesh of the spine from X-ray images;

- Developing a surrogate 3D FE model combined with a bone growth model of the spine; and
- Developing a modified bone growth model containing PS time-varying and geometry based parameters.

This dissertation proceeds as follows: in Chapter 2, image segmentation parameters are calibrated to expedite the process, and a 3D reconstruction method is used to reconstruct the geometry using X-ray data. Chapter 3 focuses on generating a detailed PS surrogate finite element model of the human spine. The machine learning method is the topic of Chapter 4, which explains how the framework can be used in conjunction with the modified bone growth model, data from the spine surrogate model, and extracted data from medical data to create the bio-informed mechanistic prognosis framework. Finally, in Chapter 5, conclusions are drawn, and future research directions are discussed.

CHAPTER 2

Patient-specific image segmentation and data generation

2.1. Introduction

To track the evolution of deformities throughout adolescent growth, frequent imaging is essential [**12**] and the extracted features from medical images such as Cobb angle determine the severity of spinal deformity. Later, these features can be implemented to classify spinal deformities based on image features [**50**]. Various imaging techniques, such as X-ray, magnetic resonance imaging (MRI), or computed tomography (CT), may be used to detect spinal deformity. Compared to MRI and computational tomography (CT) scanners, X-ray images are more commonly employed due to their accessibility, lower cost, shorter scanning time, and lower ionizing radiation levels particularly for adolescent patients. X-ray are taken from two orthogonal view known as anteroposterior (AP) and lateral (LAT) view shown in Fig. 2.1. Segmentation of images is a critical and challenging aspect of image processing [**51, 52, 21**]. Additionally, this is a barrier that impedes the deployment of 3D reconstruction as well as other innovations [**53**]. Precisely segmenting the vertebrae is critical for subsequent analysis in an injury detection system. This chapter addresses the aforementioned challenges by introducing an effective approach for segmenting X-ray images, generating 3D reconstructions of the spinal column, and extracting mechanistic features.

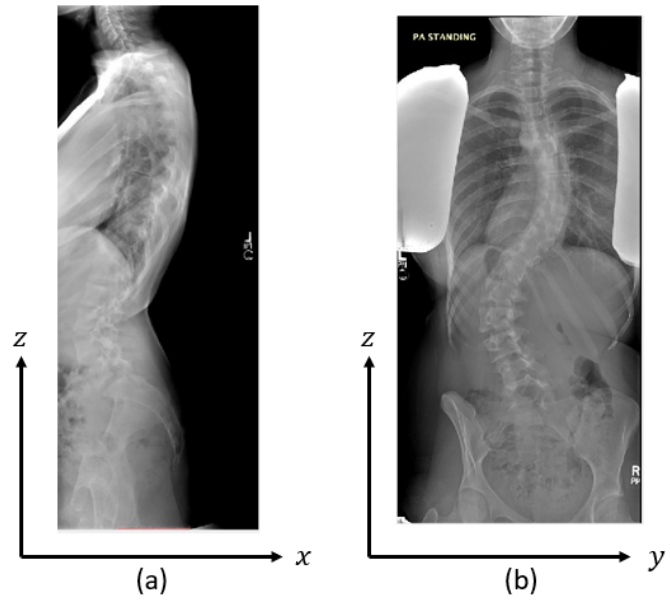

Figure 2.1. (a) Lateral (LAT) and (b) Anteposterioir (AP) view of the image obtained from X-ray data.

2.2. Data collection

To collect the imaging data for this project, we selected patients with AP thoracolumbar X-ray imaging from the radiology records of a large urban tertiary pediatric hospital (Lurie Children's in Chicago, Illinois) between September 2011 and July 2019. Demographic data was collected, along with radiographic diagnoses. Scoliotic curvature was defined as Cobb Angle $> 10^\circ$ [**54**]. Those patients with neuromuscular etiologies and structural deformities (e.g. spina bifida) were excluded. Patients were between 7 months to 21 years of age. Of those patients with radiographically diagnosed scoliosis, 190 were included with age at study ranging from 2-18 years. 130 of these patients were female. 55 of these patients had at least one level of operative vertebral fusion. 163 patients without radiographically diagnosed scoliosis met the

inclusion criteria, ranging in age from 7 months to 21 years. Of these, 83 patients were female. None underwent spinal fusion. Demographic data is shown in Table 2.1.

Table 2.1. Demographic information for the X-ray imaging data.

Features	Scoliosis	Control
Number of patients	190	163
Sex	103 Female	83 Female
Age range	2-18 years	7 months-21 years
Spinal fusion	55	0

2.3. Image segmentation and parameter calibration

In this section, we provide a detailed explanation of the process of extracting landmarks from X-ray images in order to generate patient specific geometry (Chapter 3) and to study non-uniform bone growth (Chapter 4). Image segmentation of clinical X-ray images is carried out to extract features for the prognosis framework [**55**]. The corner points of each vertebra are identified and used as reference points to monitor variations in spine shape and bone formation over time. We implement semi-automated image segmentation using active contour, also known as, the snakes method [**56**]. A rectangular contour consisting of four corner points is initialized manually around each vertebra and evolved to capture the shape. The segmentation is carried out in 2D for both AP and LAT images. The evolution of the active contour is carried out iteratively through minimization of image energy, allowing it to converge at the edges of features and external constraint energy. Snakes are considered energy-minimizing splines which are defined in a parametric form. Using $v(s) = (x(s), y(s))$ to parametrically represent the location of a snake where parameter $s \in [0, 1]$. As s

changes smoothly a closed contour on a plane is traced. The total energy functional proposed in [**56**] considers both image and constraint forces is given as

$$E(\mathbf{v}(s)) = \int_0^1 E_{int}(\mathbf{v}(s)) + E_{con}(\mathbf{v}(s)) + E_{img}(\mathbf{v}(s))\,\mathrm{d}s, \tag{2.1}$$

where $E_{int}(\mathbf{v}(s))$, $E_{img}(\mathbf{v}(s))$ and $E_{con}(\mathbf{v}(s))$ are the energy functionals associated with internal spline energy, image force and external constraint energy, respectively. The $E_{int}(\mathbf{v}(s))$ term is given as

$$E_{int}(\mathbf{v}(s)) = \alpha \mid \mathbf{v}'(s) \mid^2 + \beta \mid \mathbf{v}''(s) \mid^2, \tag{2.2}$$

where α and β are weights associated with the first and second order regularization terms which are elastic length and stiffness of the contour. $E_{img}(\mathbf{v}(s))$ is defined as

$$E_{img}(\mathbf{v}(s)) = w_{line}E_{line}(\mathbf{v}(s)) + w_{edge}E_{edge}(\mathbf{v}(s)) + w_{term}E_{term}(\mathbf{v}(s)), \tag{2.3}$$

where w_{line}, w_{edge} and w_{term} are the weighting coefficients associated with the energy functionals $E_{line} = I(x, y)$, $E_{edge} = -|\bigtriangledown I(x, y)|^2$ and $E_{term} = \frac{C_{yy}C_x^2 - 2C_{xy}C_xC_y + C_{xx}C_y^2}{(C_x^2 + C_y^2)^{\frac{2}{3}}}$, $I(x, y)$ is the image intensity, $C(x, y) = G_\sigma(x, y) * I(x, y)$ and G_σ is a Gaussian of standard deviation σ [**56**].

Active contour model is fast and is able to accurately segment each vertebra in the X-ray images. However, there are a few drawbacks. The accuracy of segmentation depends on how accurately the active contour is initialized. The optimized

parameters for the segmentation of each vertebra must be calibrated ahead of time, which is a time-consuming process. We propose an improved calibration method to obtain optimum parameters for the accurate segmentation of clinical X-ray images. The parameters of the Snake algorithm are categorized into two groups: geometric parameters and fitting parameters.

Geometric Parameters: For each vertebra, we initialize the active contour as a rectangle and define geometric parameters such as the width (w_n), height (h_n) and rotation angle (θ_n) from the horizontal axis. n is the vertebra level number where $n = 1 \sim 17$ correspond to the thoracic vertebra (T1, T2, $\cdots$, T12) and $n = 13 \sim 17$ represent lumbar vertebra (L1, L2, $\cdots$, L5). From the T1 to the L5 vertebra, we assume a linear relationship between each vertebra size and vertebra level, with L5 vertebra having the largest size. The length and width of T1 and L5 can be used to determine the corresponding length and width of other vertebrae. The user chooses three reference corner points (top right, bottom right and bottom left) for T1 (w_1 and h_1) and L5 (w_m and h_m) vertebrae as shown in Fig. 2.2(a), and the parameters for the remaining vertebrae are computed using

$$\begin{aligned} h_n &= h_1 + (\frac{h_m - h_1}{N-1}) * (n-1), \\ w_n &= w_1 + (\frac{w_m - w_1}{N-1}) * (n-1). \end{aligned} \tag{2.4}$$

For each vertebra, the user manually selects the center point. The rotation angle can be obtained by

$$\theta_n = cos^{-1}(\frac{\vec{\phi}_n.\vec{x}}{|\vec{\phi}_n|.|\vec{x}|}) \tag{2.5}$$

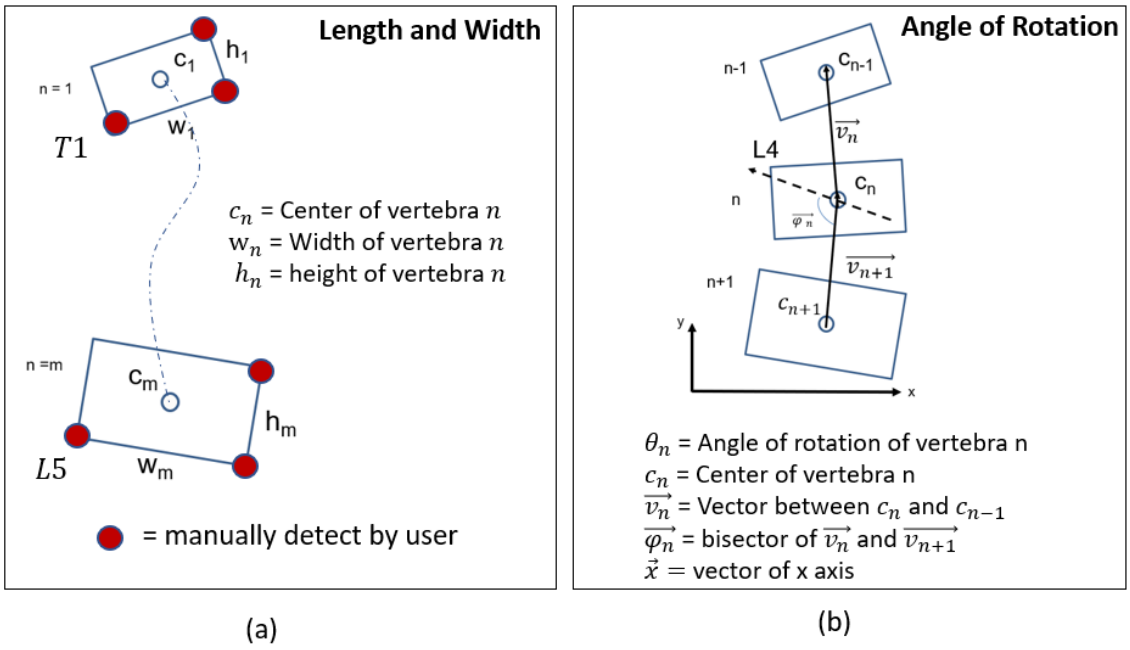

Figure 2.2. (a) Approximating length and width of vertebrae by picking reference corner points of T1 and L5; and (b) the approximation of angle of rotation for each vertebra [**1**].

where θ_n is the rotation angle of the vertebra n, $\vec{x}$ is the vector of horizontal axis and $\vec{\phi}_n$ is the bisector of the vector that connects the two adjacent vertebrae as shown in Fig. 2.2(b). It is worth noting that the framework may be used for any number of vertebrae in any regions of interest, including cervical, thoracic, lumbar, or a combination of all three. By estimating geometric parameters for the lumbar spine, Fig. 2.3 compares the ground truth and the modified snake method. The findings are in excellent accord with the ground truth, as shown.

Fitting Parameters: The weighting coefficients in the active contour model are set in order to move the contour around each vertebra. α and β are the weights associated with the first-order and second-order regularizing terms of the internal spline energy

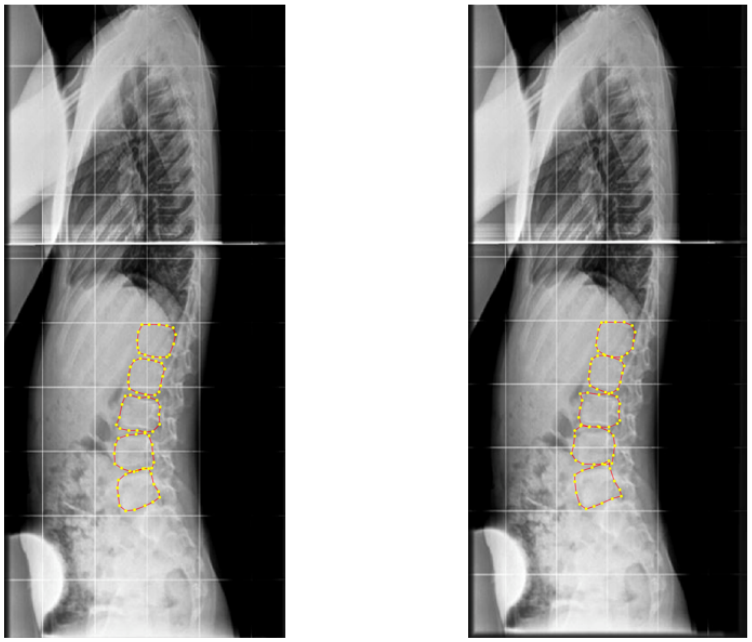

Figure 2.3. Comparison between two segmented lumbar spines using the snake algorithm, the yellow dots are the landmarks identifying the spline fitted to the boundary of vertebrae (a) ground truth (b) by estimating geometric parameters (angle of rotations, length and width of each vertebra) [**1**].

(Eq. (2) in [**56**]) that control the tension and rigidity of the snake, respectively. γ is the step size associated with the iterative update of the active contour and κ is the weighting coefficients associated with the derivatives of the external force terms (Eq. (17) in [**56**]). w_l, w_e and w_t are the weighting coefficients associated with the image, edge, and terminal energy functions, respectively [**56**]. By identifying the optimal sets of these parameters, one may precisely determine the curvature of the vertebrae. A sensitivity analysis [**57**] is performed on each pair of snake parameters, as illustrated in Fig. 2.4, to provide a better estimate on the optimized parameters. To come up with the optimized parameters throughout the dataset, the optimized pair with the

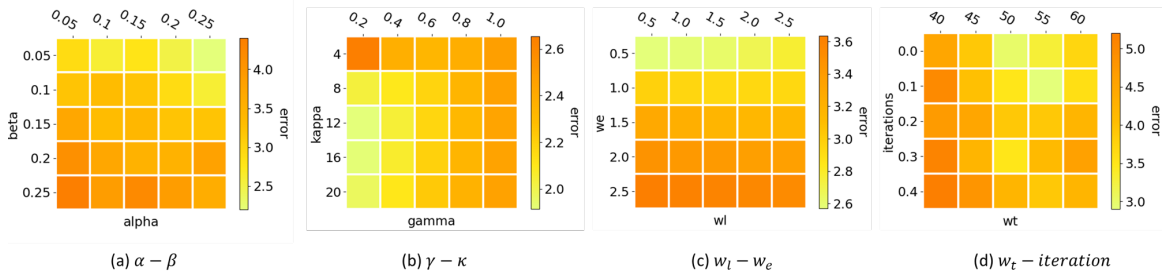

(a) $\alpha - \beta$ (b) $\gamma - \kappa$ (c) $w_l - w_e$ (d) $w_t - iteration$

Figure 2.4. Sensitivity analysis on the *calibrating parameters* of the snakes algorithm to set initial point for multi variable optimization [**1**].

least error will be picked and assigned as the initial values in the Simplex method. As a result of this phase, all of the parameters are optimized, as shown in Fig. 2.5.

Fig. 2.6 depicts the segmented spinal column in AP view, taking into account both the geometric parameters and the calibrating parameters. First, the reference point of the most top and the most bottom vertebrae will be identified and then the program will identify the contour around each vertebra.

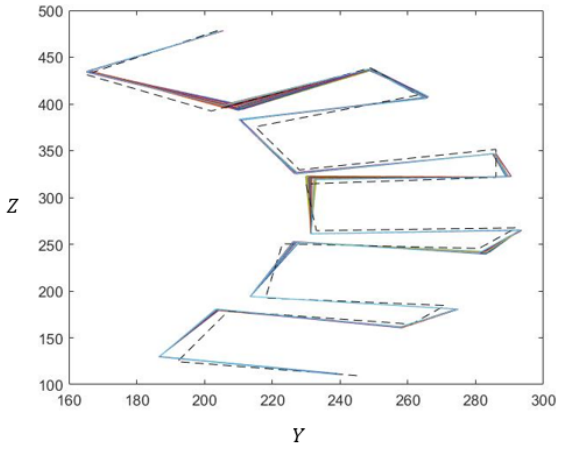

Figure 2.5. Optimized multi variables of the snakes method for the lumbar spine. The dotted line denotes the ground truth and solid lines are the optimized configuration. The normalized mean square error is 0.0187 corresponding to $\alpha = 0.25$, $\beta = 0.25$, $\gamma = 12$, $\kappa = 0.2$, $w_l = 0.5$, $w_e = 0.5$, $w_t = 0$, and $iteration = 50$.

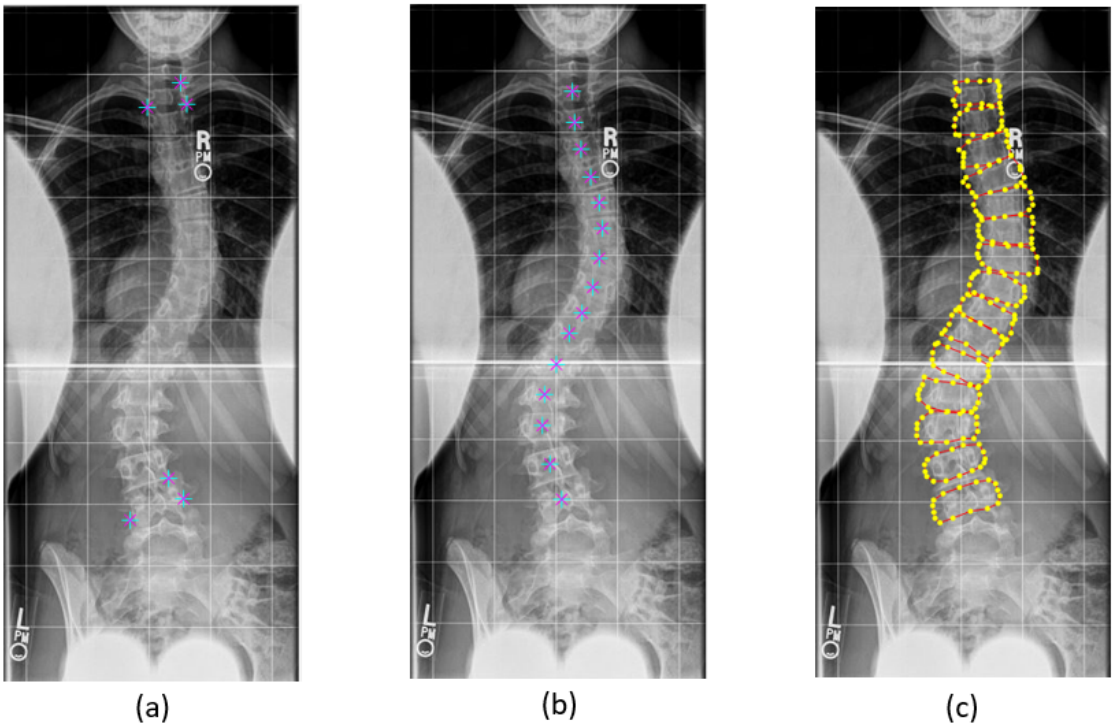

Figure 2.6. Three steps for image segmentation. (a) Picking the reference point of the most top and bottom of each vertebra, (b) pick the center point of all vertebrae and (c) segmented data by implementing optimized geometric and calibrating parameters using the snakes algorithm [**1**].

2.4. Defining spinal angles

2.4.1. Background

Spinal curvature measurement is time-consuming and unreliable in clinical practice. Radiographic criteria, particularly the Cobb angle, are used to determine whether to monitor, brace, or propose surgical intervention for scoliosis [**58**]. These measures' results have significant consequences for patient therapy and care. The Cobb technique has been considered the gold standard for determining the magnitude of a scoliosis

curve [**59**]. The Cobb technique, however, has certain drawbacks. According to studies of interobserver and intraobserver reliability, the Cobb angle has a measurement error of around 3–5° [**60, 61, 62, 63**]. An inaccurate definition of the end vertebra, an improper drawing of the lines through endplates or the pedicles, and the drawing of perpendiculars or the measurement of the angle itself are all possible sources of inaccuracy [**64**]. Anterior-posterior or posterior-anterior standing radiographs are often used to determine the Cobb angle. Scoliosis, on the other hand, is a three-dimensional (3D) deformity, while the Cobb angle recorded on an X-ray on a plane is a two-dimensional (2D) value [**65**]. Furthermore, there is no standard approach for quantifying the shape or severity of AIS cases, classifying patients, or determining the appropriate course of therapy at this time. This section aims to introduce five global angles extracted from both the AP and LAT views to quantify the 3D geometry of the spine in a unique way and provide a standard technique to compute them.

2.4.2. Assumptions

Key assumptions were used to select a coordinate system, describe input data, and define and calculate features, documented below.

Coordinate systems: To define and plot vertebrae landmarks, a 3D Cartesian coordinate system was used:

- The $X - Y$ plane represents the transverse plane
- the $X - Z$ plane represents the lateral plane
- The $Y - Z$ plane represents the anteroposterior plane.

These planes are mutually orthogonal, with the Z-axis representing the vertical direction (parallel to patient height).

Input data: To calculate features, vertebrae landmarks were extracted from the snakes algorithm explained in 2.3 in 2D views (AP and LAT). General requirements for the structure and content of input datasets were documented to ensure "Calculating AIS Features" was applicable to other datasets, ensuring it could be widely used. Vertebrae landmarks were assigned to Region 1, 2, 3, or 4 based on location, shown in Figure 2.7. It was assumed that each region represents an irregular vertebra surface and contains an arbitrary number of landmarks. The notation used in this section is described in Table 2.2.

Table 2.2. Notation table of variables used in the feed forward neural network.

Th_t	Thoracic vertebra, $t = 1, ..., 12$
Lu_l	Lumbar vertebra, $l = 1, ..., 5$
$L^i_{j,k}$	Line passing through region j of vertebra i in k view
$i = 1, ..., 17$	Vertebra number
$j = 1, ..., 4$	Vertebra region
k	Plane, typically Anteroposterior (AP) or Lateral (LAT)
L	Lumbar vertebra with maximum curvature
T	Thoracic vertebra with maximum curvature
C	Vertebra with maximum curvature (either **L** or **T**)
U	Vertebra 2 above **C**
B	Vertebra 2 below **C**

For any 2D projection:

(1) *Region 1* represents the vertebra's left surface. Corresponding landmarks and features are shown in blue.

(2) *Region 2* represents the vertebra's lower surface. Corresponding landmarks and features are shown in yellow.

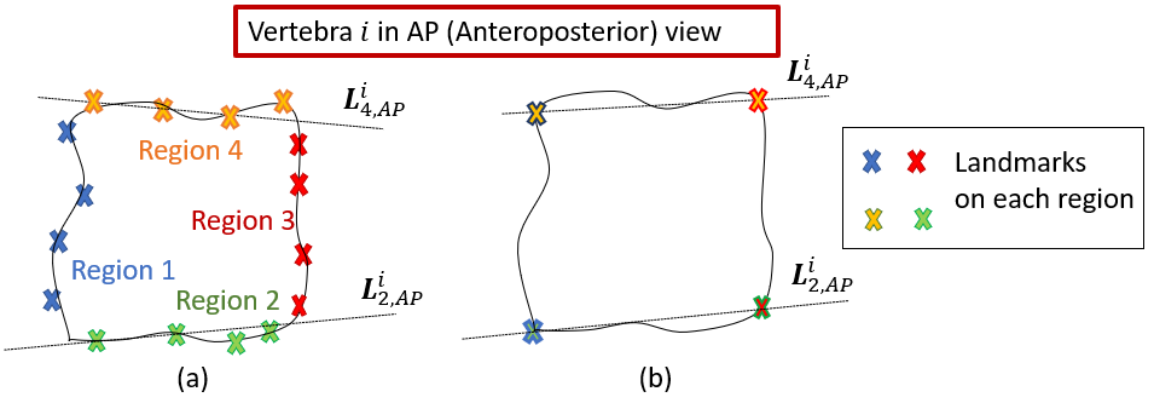

Figure 2.7. Vertebra landmarks assigned to regions 1, 2, 3, and 4, anteroposterior plane. The line of best fit through regions 2 and 4 are shown for (a) 16 landmarks and (b) four landmarks.

(3) *Region 3* represents the vertebra's right surface. Corresponding landmarks and features are shown in red.

(4) *Region 4* represents the vertebra's upper surface. Corresponding landmarks and features are shown in green.

These irregular surfaces were approximated with lines (in 2D) and planes (in 3D) of best fit. For example, Fig. 2.7 shows lines of best fit through Region 2 and Region 4 landmarks of vertebra i in the anteroposterior plane. The line passing through region j of vertebra i in k view (k can be AP or LAT) can be written as

(2.6) $$L^i_{j,k}$$

.

2.4.3. Calculating global angles

As previously discussed, there are no standard metrics to describe, classify, and compare spinal deformity patients. The spine's three-dimensional form may be represented mathematically using the following angles as shown in Fig. **??**:

- Trunk Inclination Angle (TIA) ;
- Sacral Inclination Angle (SIA);
- Thoracic Kyphosis Angle (TKA) ;
- Lumbar Lordosis Angle (LLA);
- Cobb Angle (CA).

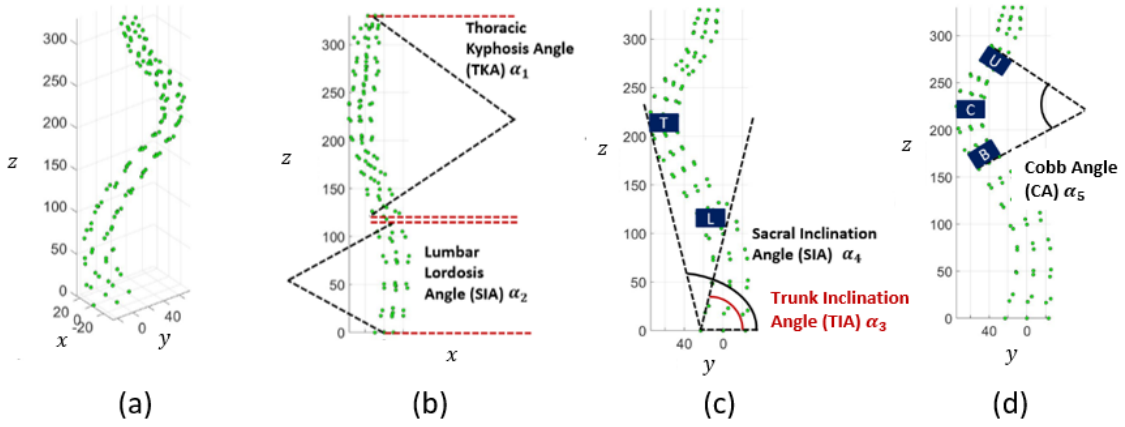

Figure 2.8. Description of the five global angles (α_i). (a) 3D configuration of the spine. The green points describe the landmarks of the spine; (b) Thoracic Kyphosis Angle (TKA) and Lumbar Lordosis Angle (LLA) in $z-x$ plane; (c) Sacral Inclination Angle (SIA) and Trunk Inclination Angle (TIA) in the $z-y$ plane; and (d) Cobb Angle in the $z-y$ plane [**2**].)

These angles are measured from 2D X-ray projections, and reflect the severity of curvature in each spinal region. This investigation proposes standard mathematical

definitions of each global angle, ensuring they are always measured relative to the same relative points.

In the lateral (LAT) plane:

- The Thoracic Kyphosis Angle (TKA) is the angle between region 2 of Th_1 (1st thoracic vertebra) and region 4 of Th_{12} (12th thoracic vertebra) calculated by

$$TKA = \cos^{-1}\left(\frac{L^{1}_{2,LAT} \cdot L^{12}_{4,LAT}}{|L^{1}_{2,LAT}||L^{12}_{4,LAT}|}\right). \tag{2.7}$$

- The Lumbar Lordosis Angle (LLA) is the angle between region 2 of L_1 (1st lumbar vertebra) and region 4 of L_5 (5th lumbar vertebra) obtained by

$$LLA = \cos^{-1}\left(\frac{L^{13}_{2,LAT} \cdot L^{17}_{4,LAT}}{|L^{13}_{2,LAT}||L^{17}_{4,LAT}|}\right). \tag{2.8}$$

In the anteroposterior (AP) plane:

- The Trunk Inclination Angle (TIA) is the angle between region 4 of L_5 (5th lumbar vertebra) and region 3 of $\mathbf{L}$ derived by

$$TIA = \cos^{-1}\left(\frac{L^{17}_{4,AP} \cdot L^{\mathbf{L}}_{3,AP}}{|L^{17}_{4,AP}||L^{\mathbf{L}}_{3,AP}|}\right). \tag{2.9}$$

- The Sacral Inclination Angle (SIA) is the angle between region 4 of L_5 (5th lumbar vertebra) and region 1 of **T** calculated by

$$SIA = \cos^{-1}\left(\frac{L^{17}_{4,AP} \cdot L^{\mathbf{T}}_{1,AP}}{|L^{17}_{4,AP}||L^{\mathbf{T}}_{1,AP}|}\right). \tag{2.10}$$

- The Cobb Angle (CA) is the angle between region 2 of **U** and region 4 of **B** explained by

$$CA = \cos^{-1}\left(\frac{L^{\mathbf{U}}_{2,AP} \cdot L^{\mathbf{B}}_{4,AP}}{|L^{\mathbf{U}}_{2,AP}||L^{\mathbf{B}}_{4,AP}|}\right). \tag{2.11}$$

2.5. 3D shape reconstruction from bi-planer 2D data

Time history X-ray images from two orthogonal perspectives (AP and LAT) are used in this study to gather PS data (Fig. 2.1). PS characteristics are retrieved from X-ray images to assess spinal deformity prognosis. The snakes algorithm, on the other hand, cannot be directly applied since the image scale varies between LAT and AP. Furthermore, there are no stable characteristics in images that can be tracked throughout time.

The initial step should be to calibrate the camera location in order to make all data consistent and comparable in scale. Here are the assumptions for the camera calibration step:

- *Reference of the coordinate system*: The coordinate system's reference point in AP and LAT perspectives is the center point of L5 (5^{th} lumbar vertebra).

- *Angle between AP and LAT views*: the angle between AP and LAT views is 90°.
- *Scaling criterion:* The images are taken with different scales. Images need to be scaled such that the heights of the spine in these two X-ray views are the same. It is assumed that AP view is fixed and the LAT view will be calibrated accordingly. The scaling factor between two pairs of images is calculated as

$$s = \frac{z_{max}^{AP} - z_{min}^{AP}}{z_{max}^{LAT} - z_{min}^{LAT}}, \tag{2.12}$$

where z_{max}^{AP} and z_{min}^{AP} are the maximum and minimum of z coordinates of landmarks in AP respectively. Similarly z_{max}^{LAT} and z_{min}^{LAT} are the maximum and minimum of z coordinates of landmarks in LAT respectively.

As seen in Fig. 2.9, the scaled data will subsequently be fed into a 3D reconstruction procedure. The size of the bounding box for each vertebra is calculated by identifying the minimum and maximum in each direction, and the nodes in 3D space corresponding to that region are identified. The nodes on the boundary and corners will also be detected using the MATLAB *convhull* function [**66**](Convex hull of the $3D$ reconstructed region). The $3D$ reconstruction geometry will be obtained as well as the boundary points and corner points for every vertebrae by performing the described technique and utilizing the scaled landmarks received from the X-ray images (Fig. 2.10).

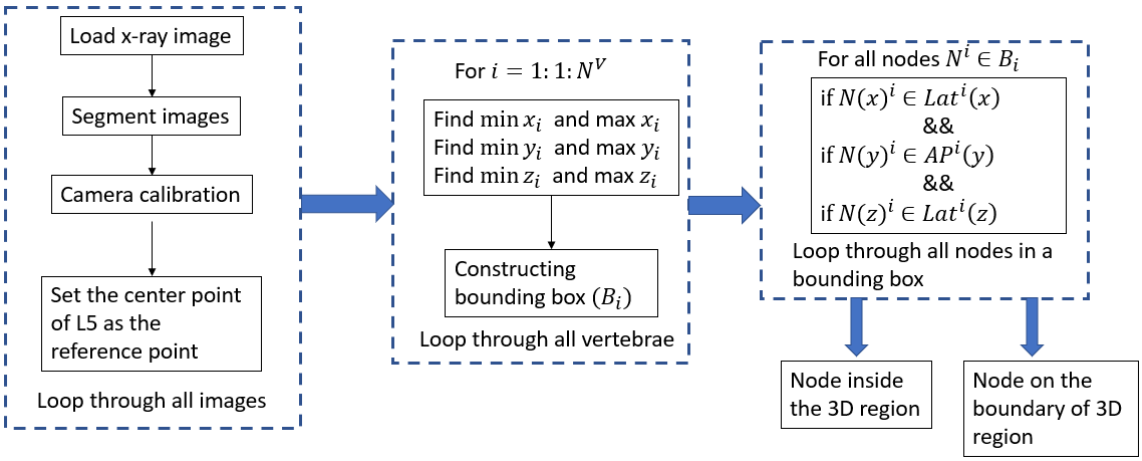

Figure 2.9. The flowchart of 3D reconstruction of vertebrae using 2D data [**1**].

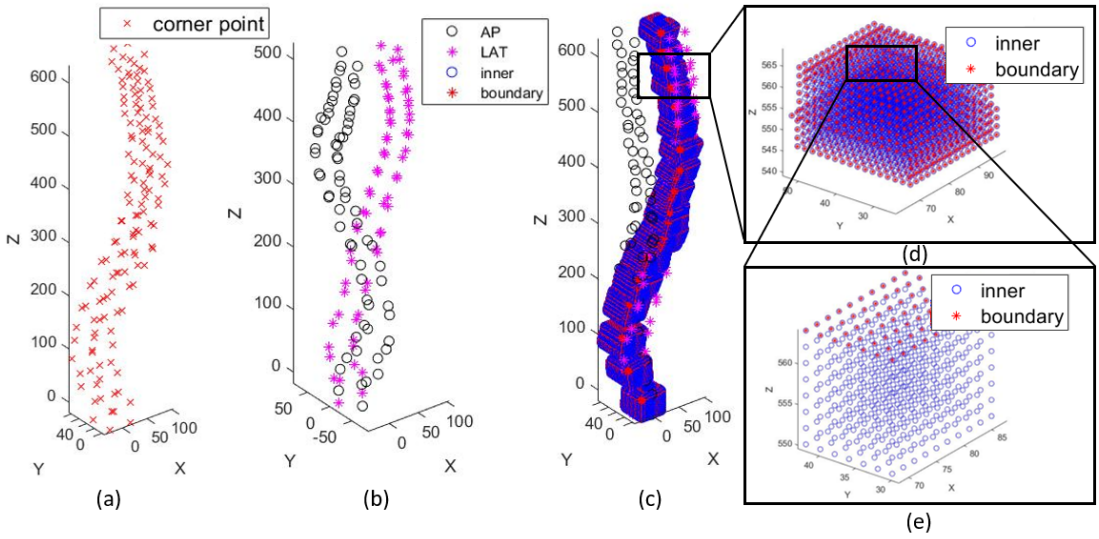

Figure 2.10. 3D reconstruction of vertebrae using 2D data. The camera parameters are calibrated before reconstruction. (a) The 3D reconstructed corner point, (b) the segmented data of the AP and LAT views, (c) the 3D reconstructed geometry using the bounding box algorithm. The red points denote the outer surface and the blue points denote the inner surface. (d) and (e) are the zoomed view of the L3 vertebra, visualizing the 3D reconstructed inner and out points [**1**].

CHAPTER 3

Generate a patient-specific surrogate spine model using imaging data

3.1. Background

In this Chapter, a surrogate spine model is developed to approximate the selected properties based on the results of the physical model. A surrogate model is the one that approximates a more complex, higher fidelity model and can be used in place of the said complex model [**67**]. Surrogate modeling is a well-known approach to study various industrial engineering problems and is a great tool to assist the computationally expensive analysis and optimization [**68**]. In this research, a surrogate spine model is introduced in which the modeling parameters are fitted to get the best result. Previous efforts on building spine models are found in [**69**], where the models are validated for single distinct spinal geometry with one set of material properties. This fact raises the question regarding the validity of the results and compatibility with the *in vitro* and *in vivo* results. As presented in Appendix A, the surrogate model is validated based on the reported range of data in the literature. It should be noted that indirect validation is used as described in [**70**] since the *in vivo* stress distribution on each distinct geometry is not available. The results obtained by the surrogate model will be used in the bio-informed mechanistic NN (Chapter 4) and will provide the "trend" of the output prediction data.

3.2. Generate patient specific volumetric mesh of spinal column and rib cage using MR data

In this section we aim to generate a detailed model of human spine and rib cage including all tissues. Human spine is a complicated 3D geometry and generating patient specific 3D mesh would be time consuming process. For different biomechanical applications and clinical assessment, three-dimensional mechanical modeling of human tissue is necessary, but repetitive manual processing of multiple images is needed [**71**]. Thanks to the registration method [**72, 73, 74**], the process of generating a detailed model can be performed once and later for other patients, the steps can be performed by obtaining a number of landmarks from X-ray data and registering them to the detailed model. This is beneficial in two major aspects. First, not all patients have the CT or MR data due to the adverse effect of radiation on the patient and the high cost of 3D imaging. Second, it is time-consuming to segment each slice of the image and assemble all the geometries. As it is described in Fig 3.1, the 3D reference model (also known as ATLAS model) is generated erstwhile using the MR/CT data from a voluntary patient. This model will be implemented as the reference model, and for other patients, the patient-specific geometry will be generated using the landmarks from X-ray data (Fig 3.2).

Figure 3.1. The steps of generating reference model using MR data (perform one time).

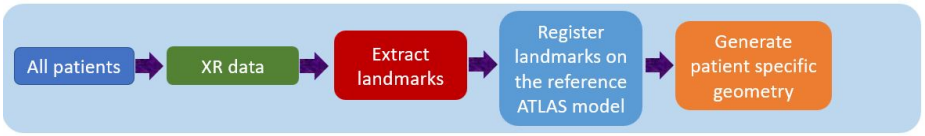

Figure 3.2. The steps of generating patient specific geometry using X-ray data (repeat several times).

3.2.1. Segmenting MR data

MR data from a voluntary AIS patient is imported to the Materialise Mimics software. The MR data contains 574 2D slices of images in the transverse plane in DICOM (Digital Imaging and Communications in Medicine) format. The DICOM images contain the patient information (i.e. age, sex, birthday and the date that the exam was taken). Fig 3.3 shows the environment of Mimics software after importing all the slices of the spine images. Mimics can provide this ability to segment each slice based on the desired tissue. Fig 3.4 shows setting up the threshold for the cortical bone, and the green area denoted the cortical bone area. Although the software has some automatic threshold for hard and soft tissue detection, it would sometimes be required to define the threshold manually to capture all the pixels corresponding to the desired tissue.

From the cortical bone region detected by the software, the area of interest (spinal column and rib cage) should be selected. Fig 3.5 shows the generated geometry by the software. The developed geometry should be post-processed to be implemented for the finite element analysis. The parts corresponding to different tissue should be separated in every slice of the image. Fig 3.6 shows the two masks, one correlated to the rib cage and the other corresponding to the spinal column. The "New Mask" tool

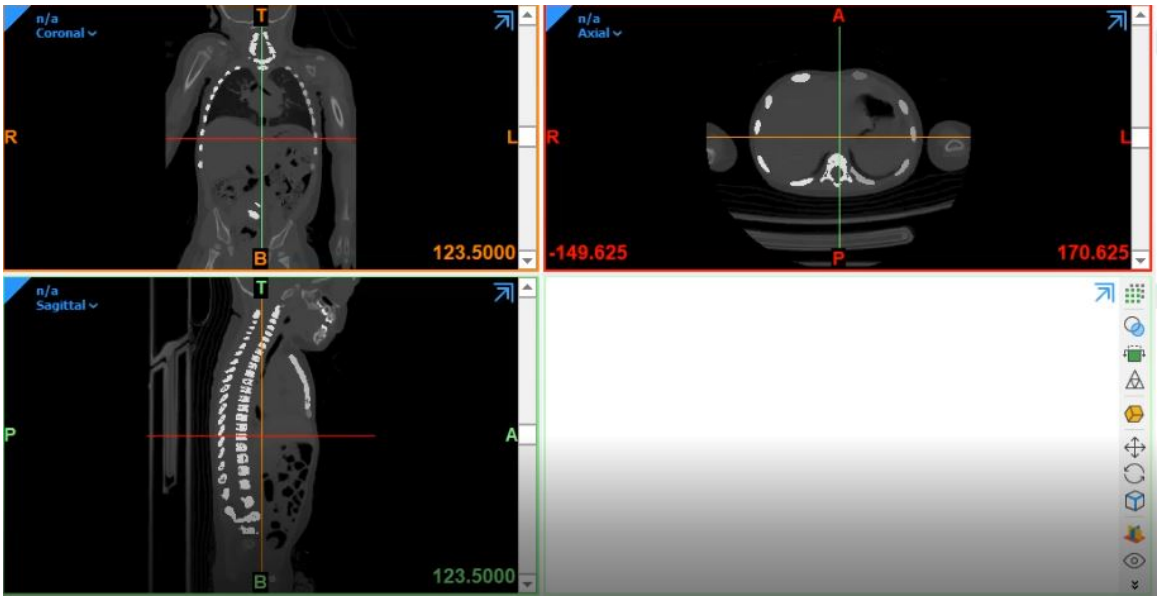

Figure 3.3. Mimics environment that visualise coronal, sagital and axial view.

can be used to highlight specific anatomy from the DICOM data. Further splitting of the masks is required to separate all tissues in every slice of the image. Fig 3.7 demonstrates splitting the rib cage mask to cartilage and the ribs. To generate the intervertebral disc, the space between the vertebrae will be filled with a volume, and the final geometry, including the vertebra, rib cage, and discs, is generated as shown in Fig 3.8.

It should be noted that the output of the Mimics is in Standard Tessellation Language (STL) format, which contains the connected triangular surface mesh. The Mimics output is imported to Trimatic Software to generate all tissue, including vertebrae cortical bone, vertebrae cancellous bone, vertebra growth plates, intervertebral disc nucleus, and intervertebral Annulus, ribs, cartilage, and sternum. The output STL file of the spine model is imported to the Meshlab Software to generate

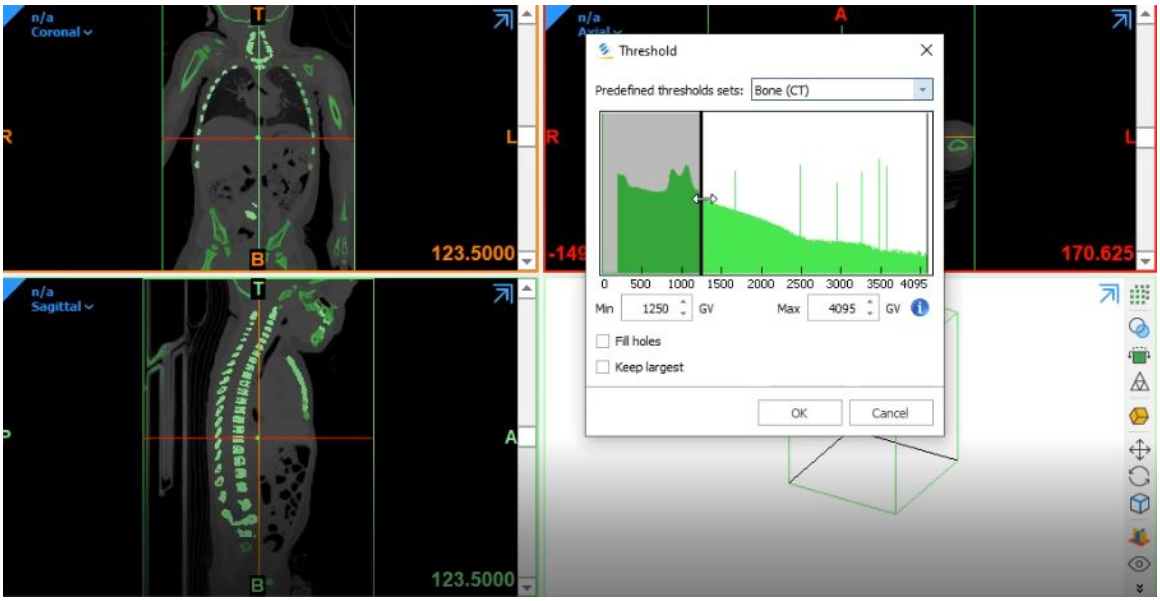

Figure 3.4. Setting up the threshold of the image to detect cortical bone.

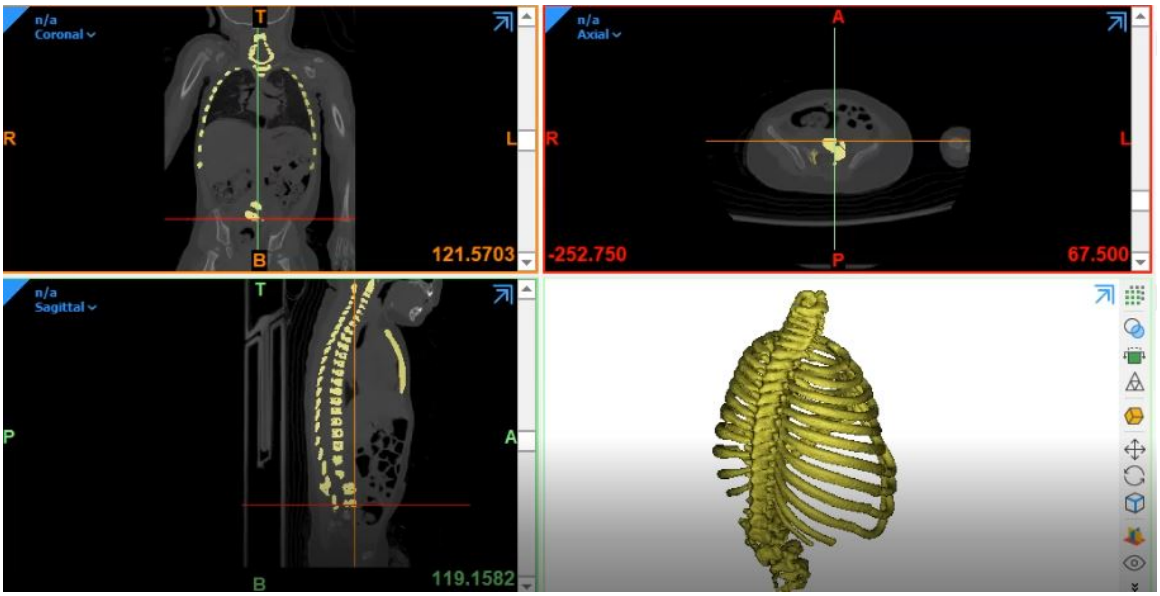

Figure 3.5. The surface mesh generated by Mimics

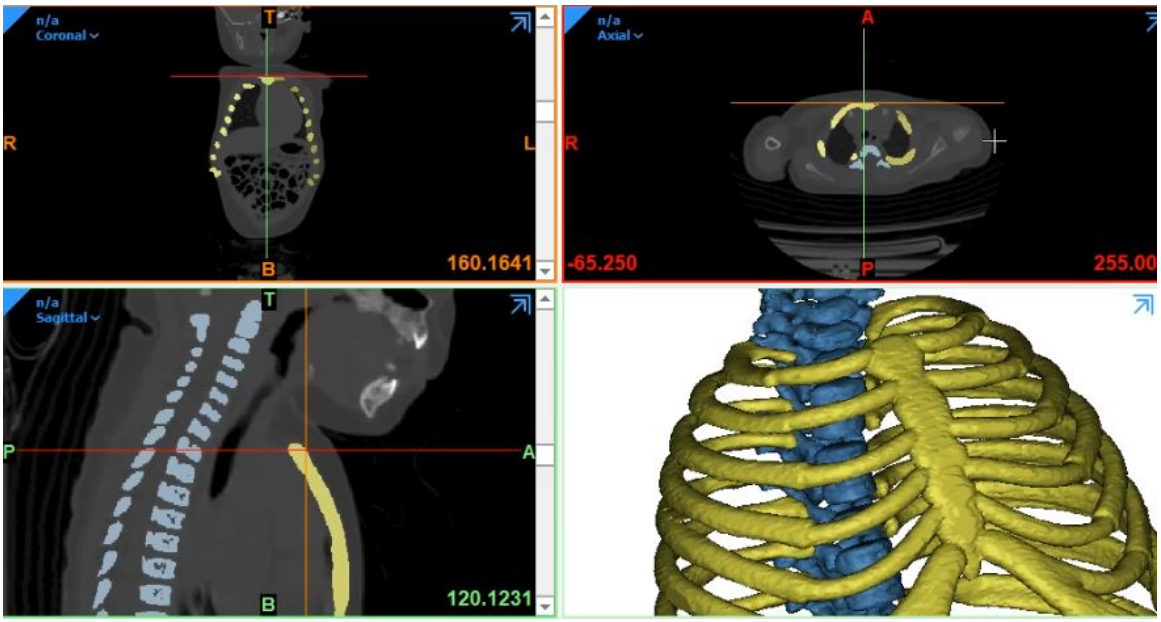

Figure 3.6. Mimics split masks to spinal column and rib cage

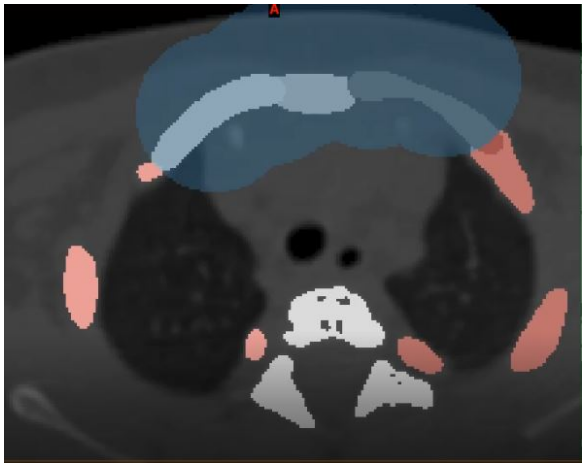

Figure 3.7. Mimics split masks to separate sternum and cartilage in the rib cage

STP file. STP stands for the "Standard for the Exchange of Product", which contains information regarding 3D objects and are typically used to transfer 3D data

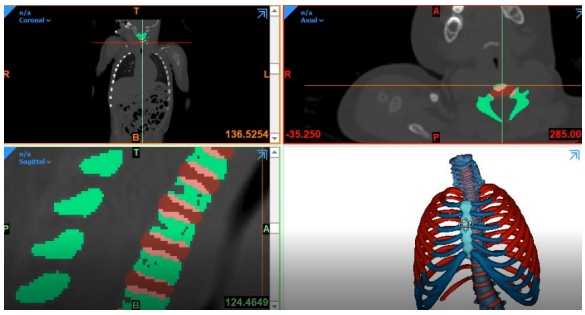

Figure 3.8. Generate intervertebral disc by filling the space between two adjacent vertebrae.

between different CAD/CAM (Computer-aided design/computer-aided manufacturing) programs. Later, the STP file is imported to Abaqus, and the mesh module of the ABAQUS is implemented to generate the volumetric mesh. Four ligaments accounting for the three major sets of ligaments (anterior longitudinal ligament (ALL) posterior longitudinal ligament (PLL) and intertransverse ligament) are defined using four spring sets. The steps are shown in Fig 3.9.

3.3. Generate a volumetric reference model of human spine

As explained in Section 3.2, the 3D finite element meshes of the vertebrae and intervertebral discs are generated using X-ray images. Each vertebra is partitioned into cortical and cancellous bone and growth plate regions and each intervertebral disc (IVD) is partitioned into annulus fibrosus and nucleous pulposes regions as shown in Figure 3.10. Linear elastic material property is considered for each tissue [**75**] as given in Table 3.1 (for 39 months) and tetrahedral elements are used for the entire spine. Since AIS targets patients in early ages, published literature proposed using a constant elastic modulus before 15 years old [**76**]. However to be more precise, the

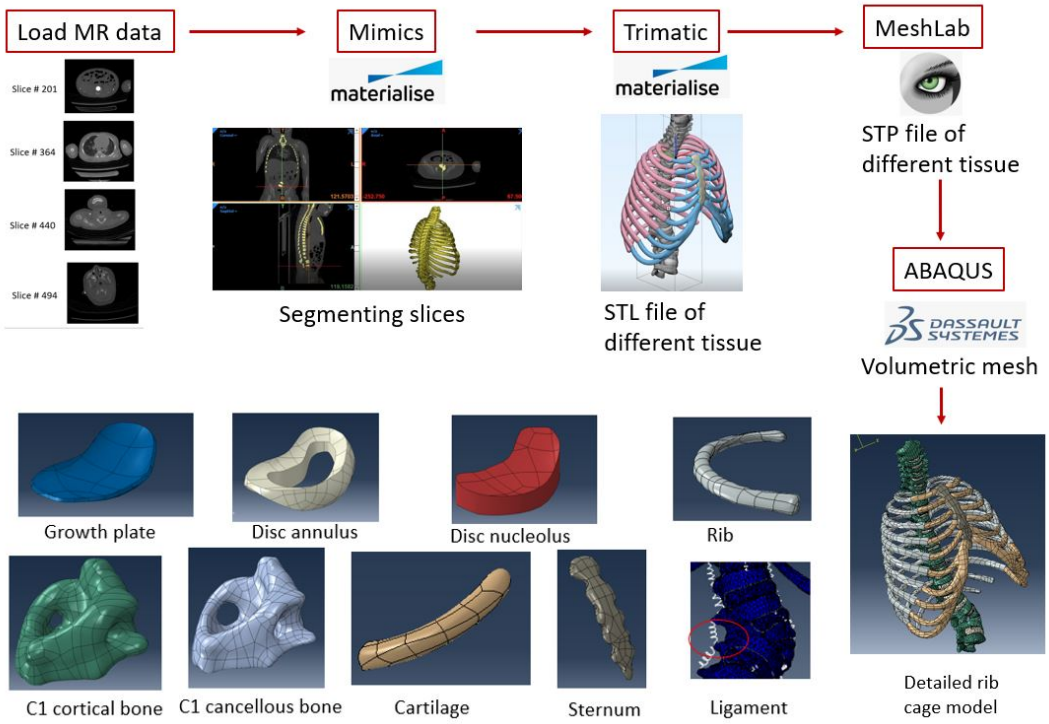

Figure 3.9. Steps to generate the reference model using MR data. In the first step the MR (or CT) data are loaded to Mimics to perform image segmenttion. Next, the generated data will be transferred to Trimatic for further improvement on the geometry an to generate the STL format. Later, the geometry will be imported to MeshLab to generate STP file. In the final step, the complted solid geometry will be import to ABAQUS for volumetric mesh, assigning time-dependent material properties and time-dependent boundary conditions.

mechanical properties of cortical bone can be updated (see Table A.2 in Appendix A) for a given year before 13 years old. In this simulation, the material properties are updated accordingly for each year. The total number of elements and vertices of the spine geometry are $595,573$ and $128,205$, respectively. The boundary conditions are defined such that the bottom surface of the L5 vertebra is fixed in all directions (X, Y and Z) and the top surface of the T1 vertebra is fixed to allow no motion in X and

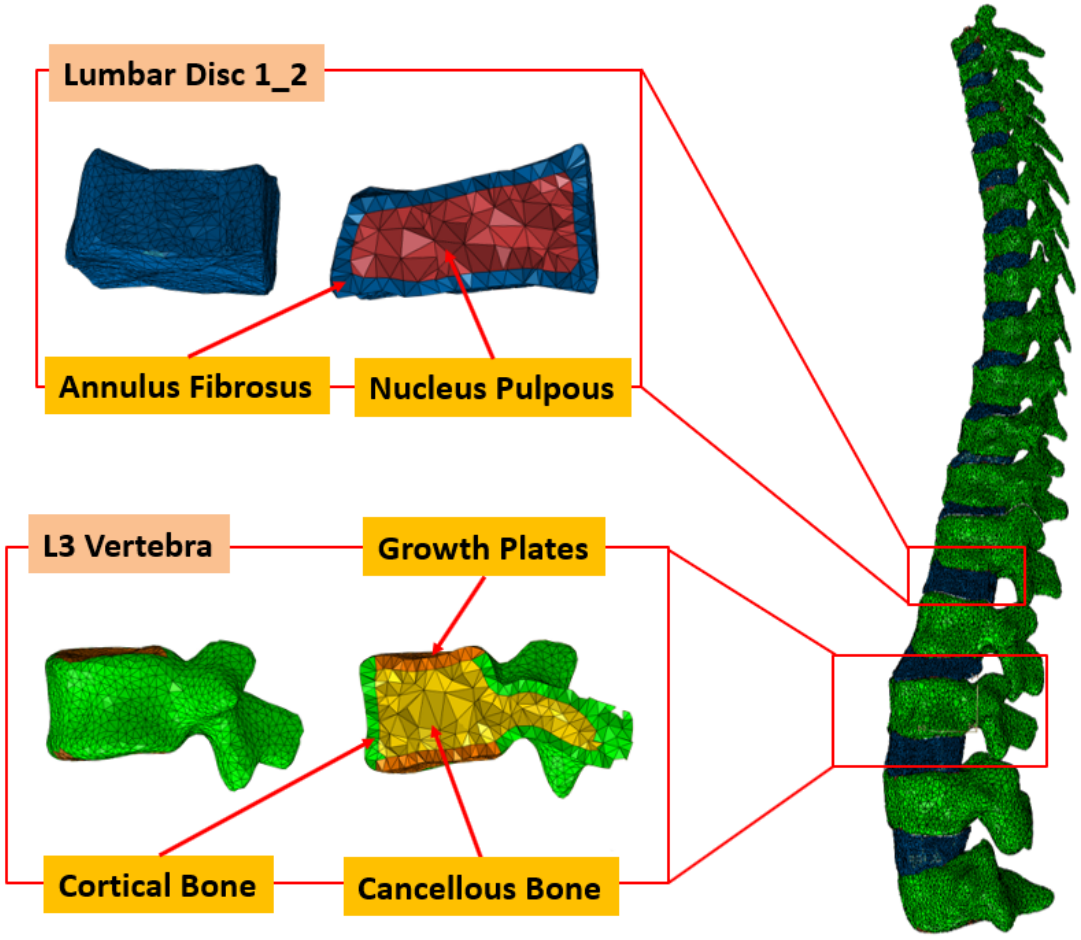

Figure 3.10. The 3D finite element mesh of the spine consisting of the lumbar vertebrae, thoracic vertebrae and intervertebral discs. The close-up views are of the partitioning of a single vertebra into the growth plate at the level of the cortical bone and cancellous bone and the intervertebral disc into the Annulus Fibrosus and Nucleous Pulposus regions are shown [**2**].

Y directions. In order to connect each intervertebral disc to the adjacent vertebrae, the nodes located on the top surface of the disc are linked to the nodes on the bottom surface of the top-adjacent vertebra. Similarly, the nodes at the bottom surface of the disc are linked to all the nodes on the top surface of the bottom-adjacent vertebra.

There are two forces applied on the spinal column. The first one is the gravitational force and the second one is the vertical stabilizing force due to the surrounding muscles of the vertebrae as it is shown in Figure 3.11. The dominant direction of the resultant loads on the spinal column is presumed to be close to the direction of the gravitational force. Gravitational load is applied at the center of mass of each vertebra and it is applied to each vertebral level unevenly based on the work proposed in [**77**]. In order to consider the effect of the surrounding muscles on the vertebral body in the standing position, the gravitational load increases as given by the equation $F^i = (15 + 2.1\, M_i)$ [**78**], where F^i is the total force applied on each vertebra v^i $(i = 1, \cdots, 17)$ and M_i is the percentage of the total mass of each vertebra as described in Table 3.2 for a subject with the weight of the spine given as 16.5 kg (at 39 months). The applied load on each intervertebral disc is calculated as $F_v^{(i,i-1)} = F^i - F^{(i-1)}$, where $F_v^{(i,i-1)}$ is the applied load on the intervertebral disc located between the vertebrae v^i and $v^{(i-1)}$. Based on the combination of gravitational and muscular forces that are calculated from the intervertebral disc pressure, this framework of calculating applied force on the spinal column is chosen such that it expresses the activity of the vertebral growth plates. The load applied to the spine can be dynamically updated based on the age and the weight can be estimated using [**5**] as described in Table 3.3.

As seen in Figure 3.12, vertebral bone has both longitudinal and lateral growth. To study the non-uniform local growth of each element, a local coordinate system is defined at each face of the tetrahedral element in which the local coordinates for one face are defined as shown in Figure 3.13. The local x and y directions are the

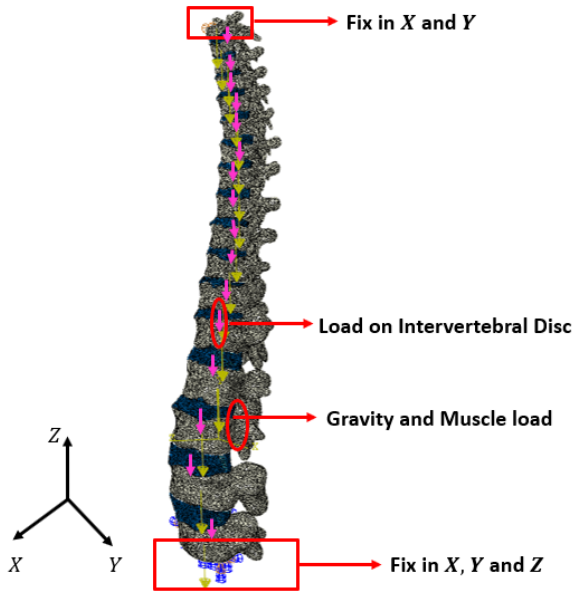

Figure 3.11. Schematic representation showing the applied gravitational and muscular load on each vertebra, applied load on the intervertebral disc and the boundary conditions for the finite element simulation [**2**].

Table 3.1. Material properties used in human spine simulation.

Tissue	Young's modulus (MPa)	Poisson's ratio
Cortical Bone	768	0.3
Cancellous Bone	400	0.3
Annulus Fibrosus	8	0.45
Nucleus Pulposus	2	0.49
Growth Plate	50	0.4

principal axes attached to each face of the elements and the local z direction is along the normal vector of the face. The origin of the local coordinate system is located at the centroid of each face. It should be noted that the corresponding elements of the surface meshes are comparable, as we are registering the volumetric mesh shown in Figure 3.10 with any new surface meshes of the vertebrae extracted from the method given in Section 3.2. Thus, the number of elements and their ID numbers are the

Table 3.2. Numerical description of the applied load ($F^i = 15 + 2.1\, M_i$) on each vertebra for the patient at 39 months (16.5 kg). Force applied to each intervertebral disc is $F_v^{(i,i-1)} = F^i - F^{(i-1)} = 0.91$ kg.

Vertebral level	Vertebral name	Percentage of total mass	Mass (M_i) (kg)	F^i (kg)
1	T1	14.0	2.31	19.85
2	T2	16.6	2.73	20.75
3	T3	19.2	3.16	21.65
4	T4	21.8	3.59	22.53
5	T5	24.4	4.02	23.44
6	T6	27.0	4.45	24.34
7	T7	29.6	4.88	25.24
8	T8	32.2	5.31	26.15
9	T9	34.8	5.74	27.05
10	T10	37.4	6.17	27.95
11	T11	40.0	6.60	28.86
12	T12	42.6	7.02	29.74
13	L1	45.2	7.45	30.64
14	L2	47.8	7.88	31.54
15	L3	50.4	8.31	32.45
16	L4	53.0	8.74	33.35
17	L5	55.6	9.17	34.25

Table 3.3. Calculating weight based on age [**5**].

Age range	Weight calculation (kg)
1	(age in months+9)/2
$(1, 5]$	2× (age in years+5)
$(5, 14]$	4× (age in years)

same for all the spine models. The z direction is calculated for the same element at three different time frames (68, 84 and 100 months). As shown in Fig. 4.4.2 a neural network will be designed which uses both clinical and synthetic (finite element simulation) data.

Based on the steps provided in 3.9 a volumetric finite element model of the spinal column and rib cage is generated. This model can be implemented later for treatment purposes. The model consists of 207,518 nodes and 752,489 elements. Four-node

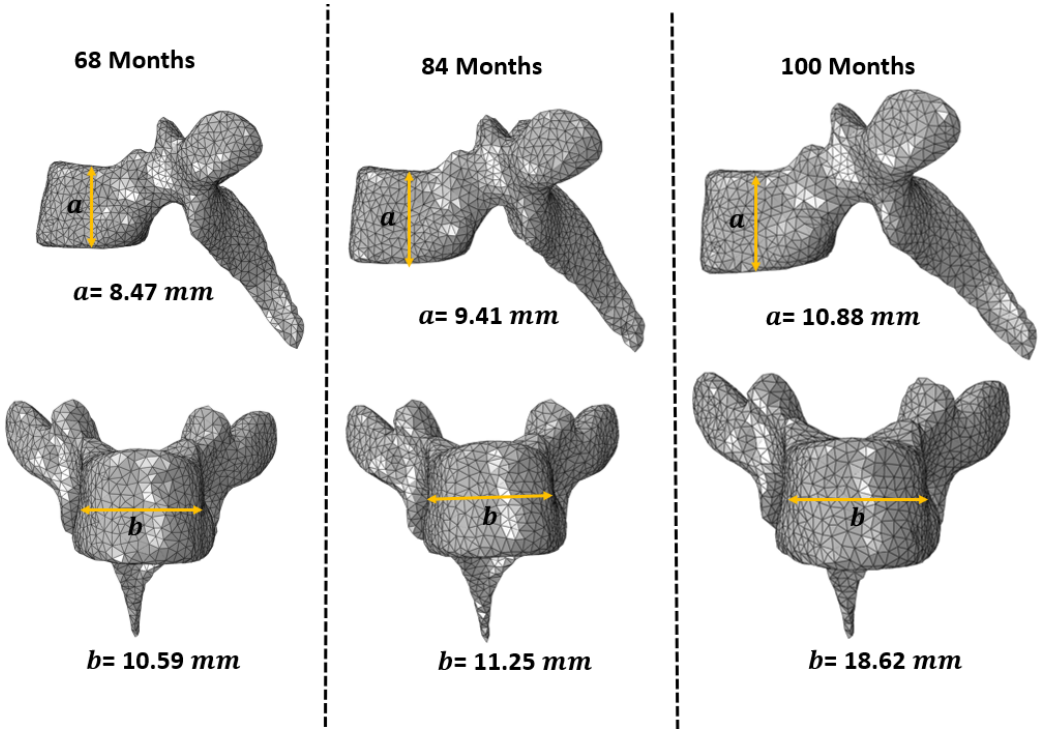

Figure 3.12. Longitudinal (a) and lateral (b) vertebral growth at 68, 84 and 100 months. The top and bottom rows show the side and front views of the volumetric meshes of vertebra, respectively.

tetrahedral element (C3D4) is used for solid sections and spring elements are used for the ligaments. The patient is a 32-month old female with the weight of 16.3 Kg. The weight of the patient can be calculated based on the age using the information provided in [**2**]. The assumptions on the weight applied on the spinal column and the mechanical properties implemented in the model is explained in [**2**]. In this model the discs are assumed to be viscoelastic and the mechanical properties corresponding the ligaments applied on the spring in the FE model is extracted from [**79**]. The displacement in the z direction is shown is Fig. 3.14 for the static loading condition.

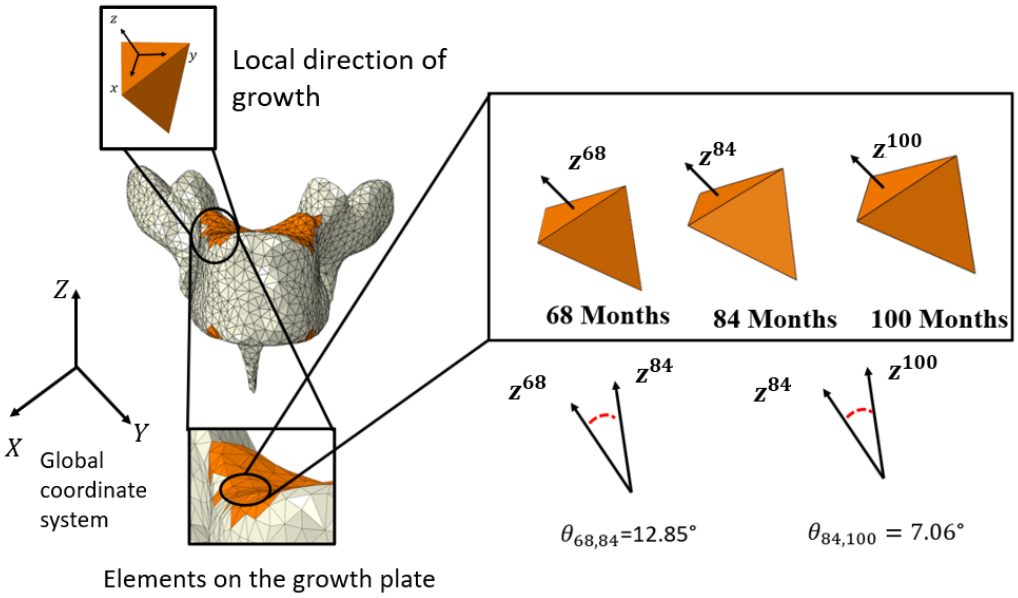

Figure 3.13. Three directions of growth are shown for one element of the volumetric mesh of a vertebra. Changes in the surface normal direction are observed between 68 and 84 months and between 84 and 100 months [**2**].

3.4. Implementing registration method to deform the reference model

Registering two surfaces involves finding a map that defines the location of semantically corresponding points between a template surface and a target surface.

In this step, X-ray data is segmented to identify the landmarks around each vertebra. Non-rigid Iterative Closest Point (ICP) is used to determine the landmarks [**80**]. In this method a search based on spatial proximity finds the correspondence of points, and the transformation of each point is modelled by general deformation. Consider Fig 3.15, the green surface is the reference surface consisting vertices v (surface S) and the goal is to reconstructing the surface passing through the vertices u which generates surface Γ. The algorithm determines the closest point (u_i) for each

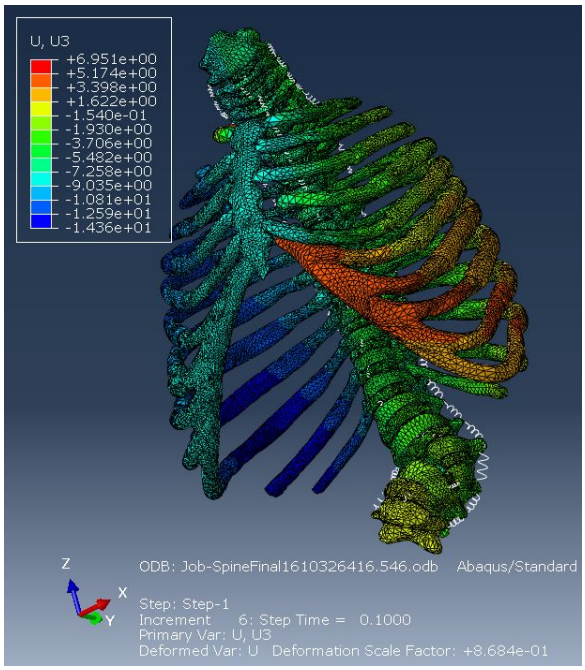

Figure 3.14. Distribution of displacement in z direction for a 38 months old patient.

displaced source vector ($X_i v_i$) and find the optimal deformation for the stiffness used in the iteration. The cost function that would be minimized in this algorithm would be

$$E = E_d(X) + \alpha E_s + \beta E_l, \tag{3.1}$$

where E_d corresponds to the distance between the target and source landmarks, E_s accounts for the transformations of neighbouring vertices. α is a regularizing term that controls the rigidity of the registration. In the case of rigid registration where the distance between the landmarks are constant in the target and reference surface,α is set to be a large value comparing to other terms. E_l explains the cost function related

to the important landmarks and the coefficient β regulates the contribution of E_l to the cost function. In this project, E_l could be selected in a way to trace the growth plates landmarks. The detailed explanation of the registration technique implemented in this project is explained in [**2**].

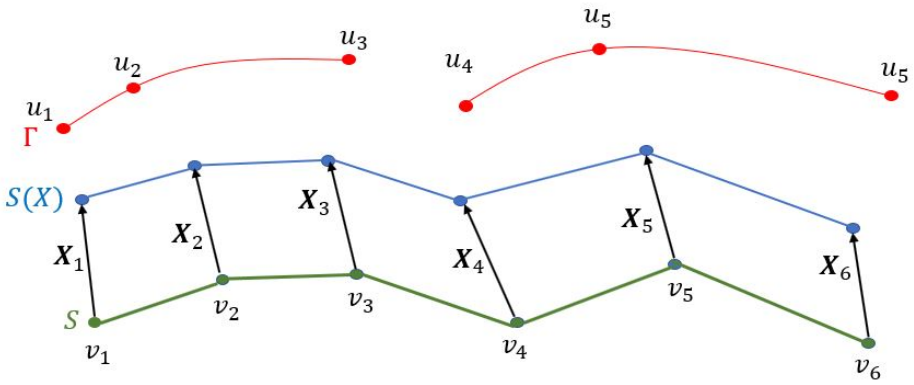

Figure 3.15. Registering the source to the target surface using ICP method. The reference surface S (green) is deformed by locally affine transformations (X_i) onto the target surface Γ (red). The algorithm determines closest points (u_i) for each displaced source vertex ($X_i v_i$) and finds the optimal deformation for the stiffness used in this iteration. This is repeated until a stable state is found.

CHAPTER 4

Mechanistic bio-informed machine learning algorithm for prognosis spinal deformity

4.1. Introducing Mechanistic Machine learning algorithm to predict spinal deformity

In chapter 2, diagnosing spinal deformity (SD) with spinal features are introduced. In this chapter we aim to introduce a methodology for SD prognosis by considering all the characteristic features. Data driven diagnosis of spinal deformities have been studied in literature to predict spinal deformities over years [**81, 82**]. However, these literature suffer from the limited training data and can only predict within the range of the input data. Rare deformities are not predicted by these models and cannot be implemented in medical application. In this chapter we bring about a data-driven bio-informed mechanistic machine learning to predict spinal deformity. Machine learning methods are known as "data-hungry" methods. Traditional data-driven approaches are regression methods that just perform interpolation on the input data. In the proposed bio-informed framework we have implemented clinical data extracted from X-ray images along with mechanistic data obtained from a spine surrogate model as the input data of the data-driven approach [**49, 2, 1**]. The clinical data are chosen in a way to uniquely characterise the 3D spinal shape discussed in chapters 2 and 3. By implementing mechanistic data in the predictive frame work one would consider the

governing physical equation of the bone growth into the predictive model to increase the accuracy of the predictive approach and enhance the predictability outside of the range of the training data. To study spinal curve progression over years, it is believed that bone growth is a crucial factor that alters vertebrae shape over years which exacerbate the spinal deformity and lead to sever spinal deformity diseases over years.

4.2. Challenges and bone growth model

Gathering all medical data, classifying them (based on age, type of deformity, and medical background), and storing them for analysis are time-consuming and labor-intensive. Furthermore, unlike traditional machine learning algorithms that require a large amount of data to train, the PS prognostic framework should be developed to meet the limited available data as well as the following challenges:

- The lack of consistent medical data for a specific person over time;
- The absence of in-vivo measurements to reveal mechanical properties of biological tissue;
- The unavailability of measuring mechanical features such as stress distribution through the whole system;
- The noises of medical images make it hard to extract meaningful information and track measurements within different time frames;
- The lack of understanding of the governing physical equations for the system;
- The inefficient process of generating detailed PS computational model that captures PS features; and

- The time difference between two consecutive data sets does not stay the same.

In the presented framework we aim at addressing the aforementioned challenges. As mentioned, traditional ML algorithms require a large amount of data to discover the system's underlying behavior. However, in the case of a PS investigation, the volume of data available for each patient is restricted, and typical ML algorithms will fail to capture the model's behavior. On the other hand, the anticipated data may be much enhanced if the governing physical equation of the system is considered since it provides insights into the expected data. However, there are several aspects to consider when employing governing physical equations. The model must be validated over a large population, and some PS time dependent constants must be calibrated for each individual patient at each time step if these models are used in computational simulations as well as ML frameworks.

The underlying physical equation that governs the progression of the spine is the bone growth model. Because AIS occurs during adolescence, when bone growth is at its peak [**83**]. It is believed that bone formation is a consequence of the stress imposed on each vertebra's growth plate [**84**] located on the top and bottom of each vertebra. On the other hand, this assumption may not be adequate to correctly depict bone growth, since other factors such as age, sex, and bone mineral density also affect bone formation. In the presented approach, we describe bone growth as follows:

$$\boldsymbol{G} = \boldsymbol{A} + \boldsymbol{B}\bar{\sigma} \tag{4.1}$$

where $\boldsymbol{G} = [G_X, G_Y, G_Z]$ are the growth rates (mm/month) along three normal directions and $\bar{\sigma}$ is the von Mises stress. Vectors $\boldsymbol{A}$ and $\boldsymbol{B}$ are PS parameters that should be calibrated for each patient, where $\boldsymbol{A} = [A_X, A_Y, A_Z]$ are considered as growth rate for non-scoliotic spine and $\boldsymbol{B} = [B_X, B_Y, B_Z]$ are the regulating growth model parameters.

4.3. Modified growth model

We aim to make the most use of all available data by exploiting medical features acquired from X-ray data, mechanistic features extracted from computational models, and addressing data scarcity while leveraging the underlying physical equation. The objective of the bio-informed mechanistic machine learning method is to reconstruct the curvature of the spine throughout time. However, the calibrated parameters generated by the system may be implemented into a computational model for monitoring and assessing bone formation on a local level.

4.3.1. Framework explanation and notation

The parameters of the physical growth equation are *patient-specific, time-dependent, and position-dependent*. Thus, Eq. (4.1) for any arbitrary landmarks on the growth plates for time t and vertebra v can be rewritten as

$$\boldsymbol{G^{tv}} = \boldsymbol{A^{tv}} + \boldsymbol{B^{tv}}\bar{\sigma}^{tv} \tag{4.2}$$

where $\boldsymbol{A^{tv}} = [A_X^{tv}, A_Y^{tv}, A_Z^{tv}]$ and $\boldsymbol{B^{tv}} = [B_X^{tv}, B_Y^{tv}, B_Z^{tv}]$ are PS time dependent, position dependent parameters that should be calibrated for each patient at a given time to

calculate growth rates $\boldsymbol{G^{tv}} = [G_X^{tv}, G_Y^{tv}, G_Z^{tv}]$ using the von Mises stress at time t for vertebra v. Indices X, Y and Z correspond to the global coordinate system shown in Fig. 2.10.

Local and global coordinate systems: To obtain the growth model parameters that correspond to the growth deformation of the vertebrae without taking into account the rigid body motion caused by the movement of the bottom vertebrae, a local coordinate system is set up at the center point of each vertebra. The axes of the local coordinates have the same direction as the axes of the global coordinate system (as mentioned in Section 3, the center of global coordinate system is at the center point of $L5$ (the fifth lumbar vertebra)). Fig. 4.1 (a) shows the global coordinate systems corresponding to the time t and the local coordinate system for the vertebra $L3$ at the same time (Fig. 4.1 (b)). The landmarks that surround each vertebra are divided into two categories: those that are positioned on the growth plates (X_G) and those that dictate the vertebra's side shape (X_S) as shown in Fig. 4.1 (c).

Growth parameters: The parameters are intended to be patient-specific, time-dependent, and position-dependent, as previously stated. The growth landmarks with comparable motion directions (due to growth) within the same vertebra should be analyzed together to represent the growth deformation of X_G landmarks. In the first step, nodes that behave similarly in each direction will be grouped together, as indicated in Table 4.1. In the y-axis, for example, landmarks 1, 3, 5 and 7 have the same growth order (positive local y), whereas landmarks 3, 4, 7 and 8 have the same growth direction in the z-axis (negative local z) as visualized in Fig. 4.2. The growth equation of each landmark (j) in local coordinates (x, y, z) for time (t) and vertebra

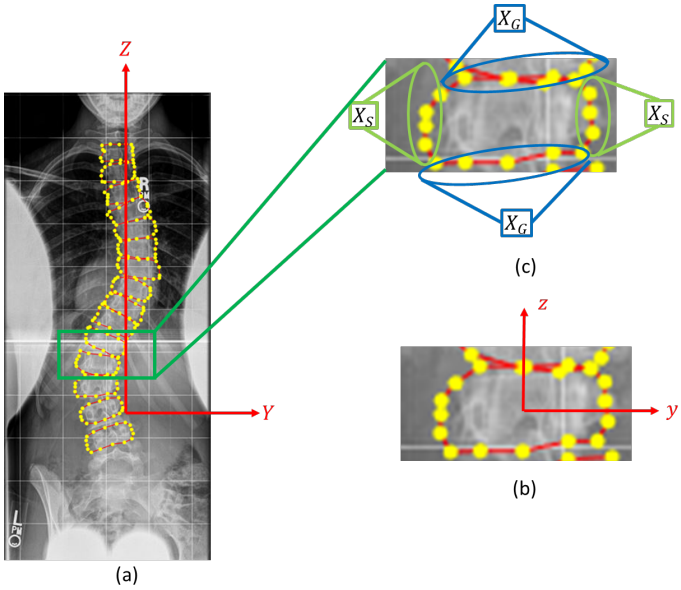

Figure 4.1. Description of the coordinate systems and landmarks. (a) Global coordinate system in AP view, (b) local coordinate system of the vertebra $L3$ in AP view and (c) labeling landmarks to growth (X_G) and side (X_S) [**1**].

Table 4.1. Landmarks with the same growth behavior are clustered into the same group.

Local growth direction	Clustered landmarks
x	$F = [1, 2, 3, 4]$ $B = [5, 6, 7, 8]$
y	$R = [1, 3, 5, 7]$ $L = [4, 2, 6, 8]$
z	$U = [1, 2, 5, 6]$ $D = [3, 4, 7, 8]$

(v) can be written as:

$$\boldsymbol{G_j^{tv}} = \boldsymbol{A_j^{tv}} + \boldsymbol{B_j^{tv}} \bar{\sigma}_j^{tv} \tag{4.3}$$

where $\boldsymbol{A_j^{tv}} = [A_{x_j}^{tv}, A_{y_j}^{tv}, A_{z_j}^{tv}]$ and $\boldsymbol{B_j^{tv}} = [B_{x_j}^{tv}, B_{y_j}^{tv}, B_{z_j}^{tv}]$ are PS time dependent, position dependent parameters for landmark (j) that should be calibrated for each patient at a given time for every vertebra and for every landmark point. Indices x, y and z

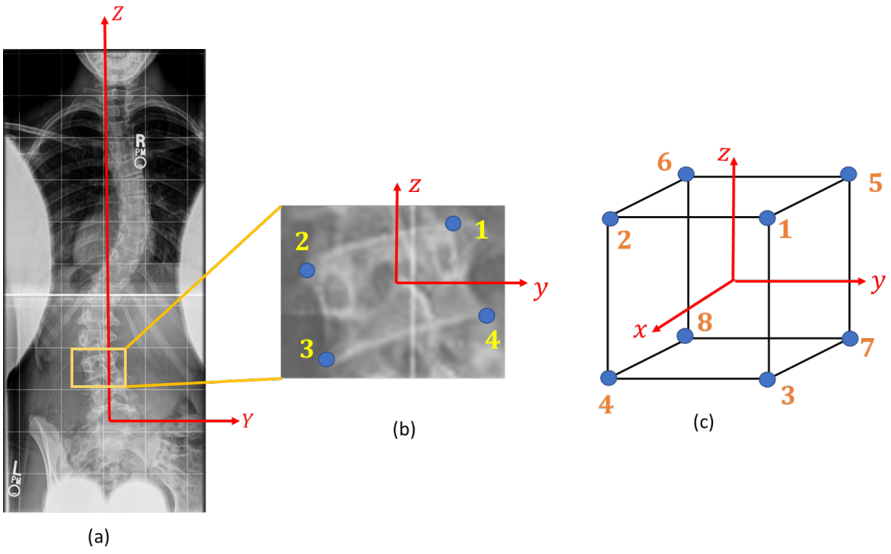

Figure 4.2. (a) Global coordinate system in AP view, (b) labeling of the growth landmarks on vertebrae in local coordinate system in 2D view, (c) labeling of the growth landmarks on vertebrae in local coordinate system in 3D view [**1**].

represent the three directions of local coordinate system shown in Fig. 4.2. It should be noted that $\bar{\sigma}_j^{tv}$ is the von-Mises stress on landmark j of the vertebra v at time t which is independent of the coordinate system. Detailed explanation on calculating growth parameters is explained in App. B.

4.4. Spinal deformity prognosis framework

A bio-informed machine learning framework is introduced in the proposed framework by incorporating our knowledge from clinical data (X-ray images) and the modified bone growth computational model explained in section 4.3. The neural networks notations are introduced in Table 4.2.

Table 4.2. Notation table of variables used in the feed forward neural network.

t	Counting index for number of time steps
$\boldsymbol{I_s^t}$	Vector of input , $s = 1, ..., N_T$
$I_{j,s}$	jth entry of I vector of input , $s = 1, ..., N_T$
$\boldsymbol{O_s^t}$	Vector of output , $s = 1, ..., N_T$
s	Counting index for number of samples (training or validation, depending on context)
m	Counting index for number of landmarks on each vertebra
N_m	Number of landmarks on each vertebrae
l	Counting index for number of layers
i	Counting index for neurons in a given layer
j	Counting index for neurons in another layer
N_T	Number of training samples
N_L	Number of layers in the neural network
$N_N(l)$	Number of neurons in layer l
$a_{j,s}^l$	Neuron value for j^{th} neuron in l^{th} layer and for s^{th} sample
W_{ji}^l	Weight connecting the i^{th} neuron in layer l to the j^{th} neuron in layer $l+1$
b_j^l	Bias of the j^{th} neuron in layer l
$\mathscr{A}$	Activation function
$\mathscr{F}_{FFNN}$	Feedforward neural network function
$\mathcal{H}$	The height of the spine

4.4.1. Feed forward neural networks

4.4.2. Machine learning framework explanation

In order to illustrate the structure of feed forward neural networks (FFNNs), a simplified one-dimensional example is presented. In the proposed chapter, we aim at predicting spine shape using the PS clinical and mechanistic features. The landmark position $\boldsymbol{X}$ is related to the features $\boldsymbol{I}$ at a given time by an unknown bio-physics equation which can be generically defined as a mapping. The overall structure of a neural network can also be described as a mapping, i.e.:

$$\begin{cases} Unknown\ bio-physics\ equation: \ \boldsymbol{X} = \mathscr{F}_{Unknown-BioPhy}(\boldsymbol{I}) \\ Neural\ network\ mapping: \ \boldsymbol{X} = \mathscr{F}_{FFNN}(\boldsymbol{I}) \end{cases} \tag{4.4}$$

where $\mathscr{F}_{FFNN}$ is the feed forward neural network (FFNN) that uses clinical and mechanistic features $\boldsymbol{I}$ as input, and generates landmark coordinates $\boldsymbol{X}$ as the output. The structure of a simple FFNN is shown in Fig. 4.3(a). The notation used in this figure and throughout this section is defined in Tab. 4.2. For this illustration case, only one sample in 1D is considered, hence $s = 1$ and all variables are written without the superscript s. A general FFNN contains neurons (the circles) and weights (black lines).

In general, an FFNN has one input layer, one output layer, and multiple hidden layers. Each layer may have multiple neurons; for the input and output layers, these are simple the input and output values. In the simplest case, an FFNN would have one input neuron, one hidden neuron, and one output neuron. To predict the position of a landmark, the input neurons would be clinical and mechanistic features, the hidden neurons would act as a multiplicative, functional decomposition of the unknown bio-physics equation that estimates the unknown function required to map input features to coordinates in the output neurons. Generalizing this slightly, we might consider an FFNN with three hidden neurons, as shown in Fig. 4.3. Each neuron has only one value. The first neuron is the input features I :

$$a_{i=1}^{l=1} = I \text{ (input layer)} \tag{4.5}$$

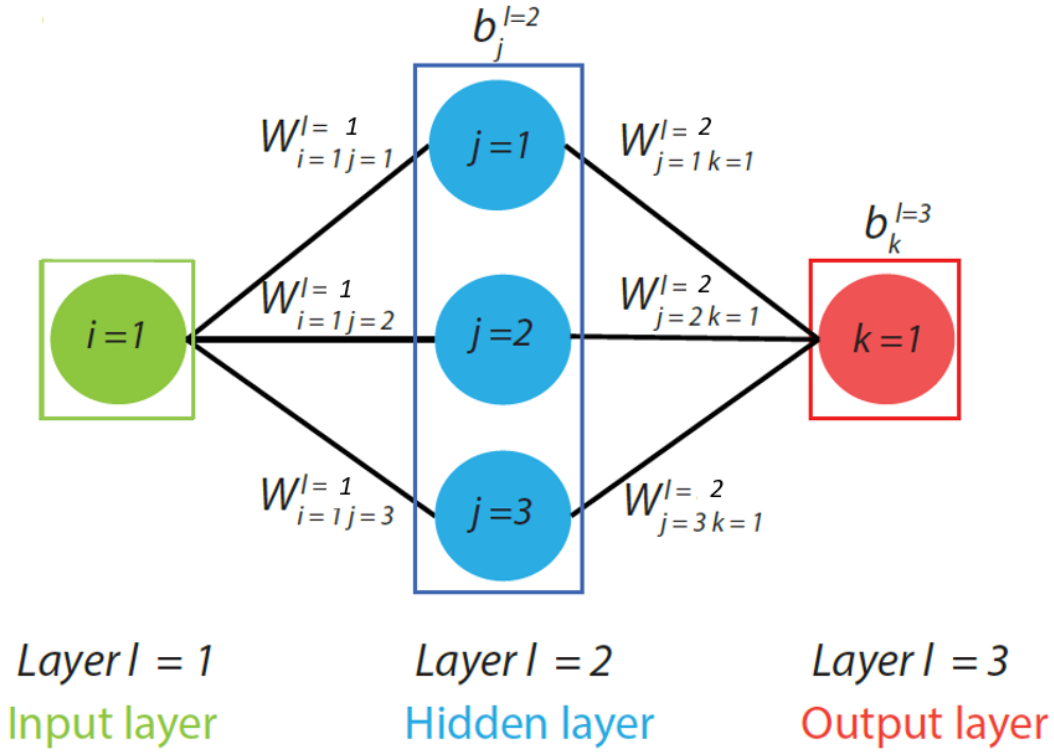

Figure 4.3. Illustration of an FFNN network with one hidden layer; the collective function of the weights and biases connecting the input layer (green), the hidden layer (blue), and the output layer (red) is estimating the unknown governing bio-physics equation [**3**].

The three neurons in the hidden layer take in this value, and each take on the value given by:

$$a^{l=2}_{j=1,2,3} = \mathscr{A}(b^{l=2}_j + \sum_{i=1}^{1} W^{l=1}_{ij} a^{l=1}_i) \text{ (hidden layer)} \tag{4.6}$$

where $\mathscr{A}$ is an activation function. In the training part, this research uses ReLU (Rectified Linear Unit) function defined as the positive part of its argument, [**85**]: $f(x) = x^+ = max(0, x)$, and each neuron is computed using a different weight $W^{l=1}_{ij}$

and bias $b_j^{l=2}$, where i is the neuron in the previous layer (in this case, the input later) and j is the neuron in the current layer (in this case, the hidden layer). Finally, the overall response – the predicted landmark coordinates – is given by:

$$X^{predicted} = a_{k=1}^{l=3} = b_k^{l=3} + \sum_{j=1}^{3} W_{jk}^{l=2} a_j^{l=2} \text{ (output layer)} \tag{4.7}$$

The combination of all the W and b terms, as well as the activation function, work as the fitting factors in a regression analysis. The activation function $\mathscr{A}$ is fixed for all neurons, and is used to condition the weighting factors. Another example shown in Fig. 4.4 extends the previous example to consider a multi-dimensional input and output, with many neurons per layer and several layers. The inputs can be defined as I_1, I_2 and I_3 corresponding PS features extracted from images and mechanistic model such as coordinates and global angles explained in chapter 2. The outputs are the three components of the predicted landmarks as X_1, X_2 and X_3. The samples from the database outlined above are used to train the neural network. After training, the FFNN can predict landmark coordinates when given corresponding inputs. In this project, MATLAB is used to build the FFNN and to train the neural network parameters [**86**].

Each neuron within every layer of a generic FFNN receives the output value from each neuron in the previous layer as input and produces a single output. This procedure is carried out for each layer. For an arbitrary number of layers and neurons per layer, the value of the j^{th} neuron in layer l for the s^{th} sample (either a training sample or prediction) may be written as:

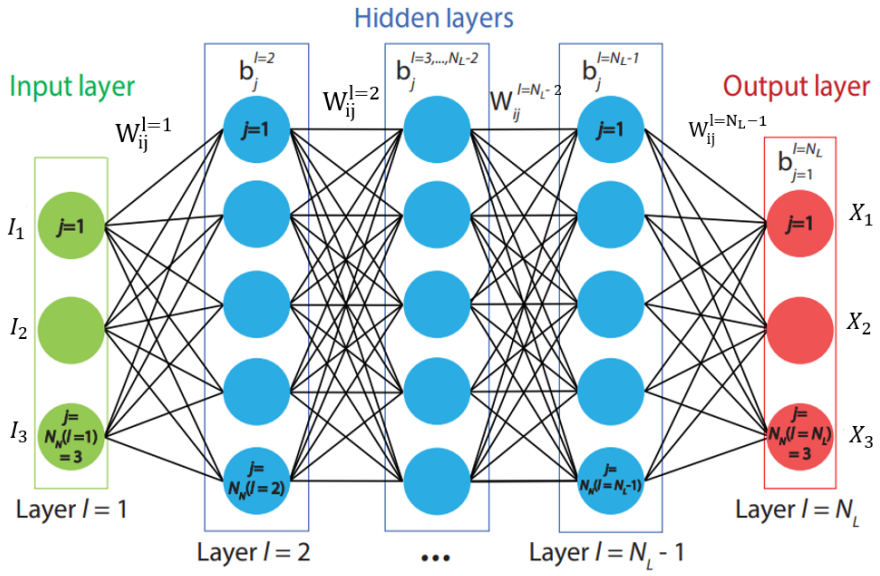

Figure 4.4. Illustration of an FFNN with multiple hidden layers; N_L: index of layers, $N_N(l)$: number of neurons in layer l. The formulation of the FFNN is given in Eq. (4.8) with associated interpretation of the FFNN structure. The indices i and j representing neuron id in previous layer and current layer, e.g., $\mathrm{W}_{12}^{l=1}$ is the weight between neuron 1 in layer $l = 1$ and neuron 2 in layer $l = 2$ [**3**].

$$a_{j,s}^{l} = \begin{cases} I_{j,s}, \text{ if } l = 1 \text{ (input layer)} \\ \mathscr{A}(b_j^l + \sum_{i=1}^{N_N(l-1)} W_{ji}^{l-1} a_{i,s}^{l-1}), \text{ if }, l \in \{2, ..., N_L - 1\} \text{ (hidden layers)} \\ b_j^l + \sum_{i=1}^{N_N(l-1)} W_{ji}^{l-1} a_{i,s}^{l-1}, \text{ if } l = N_L \text{ (output layer)} \end{cases} \tag{4.8}$$

where the final layer gives the estimated stress:

$$X_{j,s}^{\text{predicted}} = a_{j,s}^{N_L}. \tag{4.9}$$

The outputs $a^l_{j,s}$ of each layer possesses similar physical meaning as explained for the simplified case with one input and one output. The input feature components are represented by $l = 1$,$a^l_{j,s}$ for the s^{th} sample, and $l = 2, ..., N_L - 1$, $a^l_{j,s}$ represents an estimate of the the predicted landmarks. The hidden layers take in input features components and produce a estimate of the non-linear landmark coordinate responses by implementing the activation functions and weights of layer $l = 1, ..., N_L - 1$. During the training process, the non-linear unknown relationship between landmark coordinates and input features is gradually "learned" by those hidden layers. In the last layer, $l = N_L$, $a^l_{j,s}$ represents the predicted landmark coordinate.

The predicted result are produced through the regression operation in the output layer, as shown in Eq. (4.8). The weights and bias of the output layer correct the prediction generated from hidden layers, and produce accurate responses. The FFNN can learn the unknown governing bio-physics governing equation based on the loss function, input and output features. The loss function can be defined in a way to train the FFNN in a way to provide accurate estimation while providing patient specific parameters that can be considered as the hyper parameter of the network. In the following section, multiple FFNN approaches are described by implementing different loss function and different input-output features .

4.4.3. Feed forward neural network explanation with patient-specific database generated

3D-Clinical Neural Network ($FFNN_{CL}$): Given the coordinates of a vertebra's landmarks at time t, the clinical neural network attempts to predict the vertebra's

landmark coordinates at time $t + \Delta t$; see Fig. 4.5. The input vectors are $\boldsymbol{I}_s^t = [\bar{\boldsymbol{X}}_s^t, \boldsymbol{\alpha}_s^t, t, \Delta t]$, where $\bar{\boldsymbol{X}}_s^t$ indicates the landmark coordinates of sample s at time t and $\boldsymbol{\alpha}_s^t$ denotes the global angles characterizing the 3D shapes of the spine at that time. The outputs are vectors $\boldsymbol{O}_s^t = [\boldsymbol{X}_s^{t+\Delta t}]$, where $\boldsymbol{X}_s^{t+\Delta t}$ denotes the expected 3D coordinates of the vertebra's corner points at time $t + \Delta t$. The corresponding equations are explained in App. C. The relative approximation error for this model is calculated as

$$\delta_{CL} = \frac{1}{\mathcal{H}.N_T.N_m} \sum_{s=1}^{N_T} \sum_{m=1}^{N_m} \left\| \boldsymbol{X}_{sm}^{t+\Delta t} - \bar{\boldsymbol{X}}_{sm}^{t+\Delta t} \right\|^2, \tag{4.10}$$

where δ_{CL} denotes the relative error of the clinical neural network, $\boldsymbol{X}_{sm}^{t+\Delta t}$ is the coordinates of the landmark m of vertebra s predicted by the neural network, and $\bar{\boldsymbol{X}}_{sm}^{t+\Delta t}$ is from clinical dataset.

Center Point Predictor Neural Network ($FFNN_{CR}$): Given the set of landmarks' coordinates $\bar{\boldsymbol{X}}_s^t$, global angles $\boldsymbol{\alpha}_s^t$, and von Mises stress $\bar{\boldsymbol{\sigma}}_s^t$ at landmarks at time t, $FFNN_{CR}$ predicts the coordinates of the center of the sample at time $t + \Delta t$; see Fig. 4.6. More formally, the input to $FFNN_{CR}$ is $\boldsymbol{I}_s^t = [\bar{\boldsymbol{X}}_s^t, \boldsymbol{\alpha}_s^t, t, \Delta t, \bar{\boldsymbol{\sigma}}_s^t]$ and its output vector is $\boldsymbol{O}_{CR,s}^t = [\boldsymbol{C}_s^{t+\Delta t}]$, where $\boldsymbol{C}_s^{t+\Delta t}$ denotes the center coordinates of the sample s at time $t + \Delta t$. The results of this network is used to 3D reconstruct the geometry. Synthetic data is created to achieve a more accurate result, and 20% of it is used in the training step.

Bio-informed Clinical Neural Network ($FFNN_{BC}$): Using the clinical data to predict bone growth parameters, $FFNN_{BC}$ predicts the parameters of the physical growth equation given the set of landmark coordinates, global angles, and von Mises

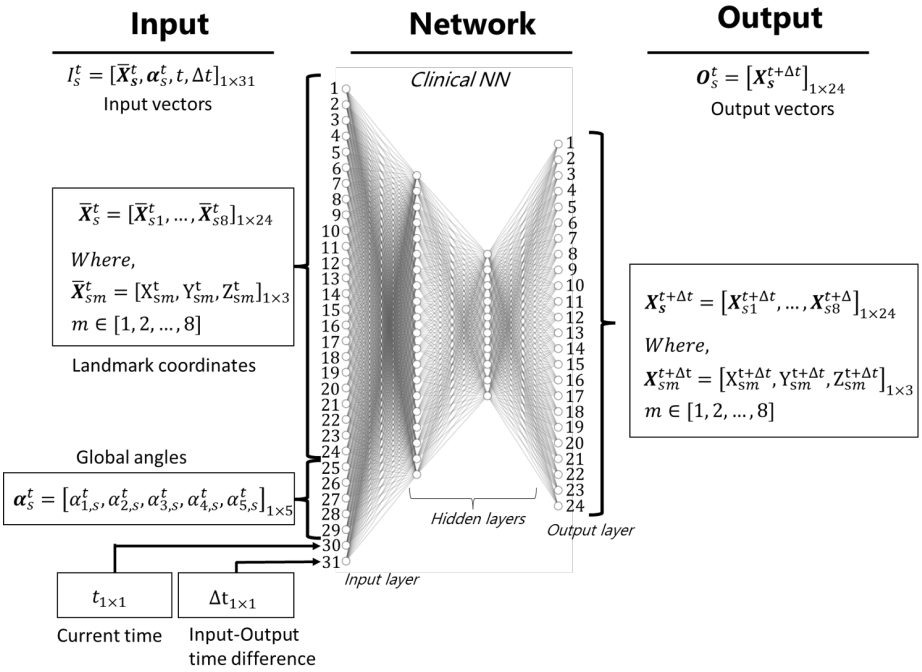

Figure 4.5. The structure of the 3D-clinical feed forward neural network $FFNN_{CL}$ developed to predict the coordinates of the landmarks at time $t + \Delta t$ [**1**].

stress at the landmarks; see Fig. 4.7. Input vectors are $\boldsymbol{I}_s^t = [\bar{\boldsymbol{X}}_s^t, \boldsymbol{\alpha}_s^t, t, \Delta t, \bar{\boldsymbol{\sigma}}_s^t]$, where $\bar{\boldsymbol{X}}_s^t$ is the landmarks' coordinates at time t, $\boldsymbol{\alpha}_s^t$ is the set of global angles, and $\bar{\boldsymbol{\sigma}}_s^t$ is the set of Von Mises stress. The outputs of the network are vectors $\boldsymbol{O}_s^t = [\boldsymbol{A}_s^{t+\Delta t}, \boldsymbol{B}_s^{t+\Delta t}]$ predicting the growth model parameters in $3D$ for each landmark. Combining the results of $FFNN_{BC}$ with the center points resulted from $FFNN_{CR}$, we are able to predict the coordinates of the landmarks of the sample at time $t + \Delta t$. The corresponding algorithm is explained in App. C.

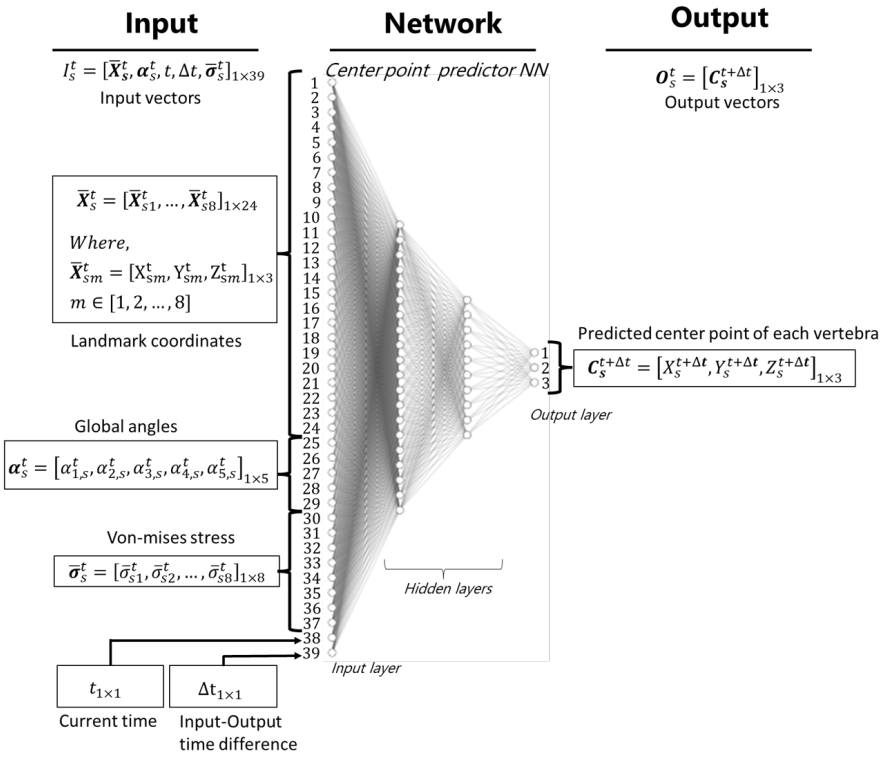

Figure 4.6. The structure of the center point prediction feed forward neural network $FFNN_{CR}$ developed to predict the location of the center point of the vertebra at time $t + \Delta t$ [**1**].

For any sample s and any landmark m on s, define the landmark $\boldsymbol{X}_{BC}^{t+\Delta t}$ predicted by $FFNN_{BC}$ as

$$\boldsymbol{X}_{BC}^{t+\Delta t} = \bar{\boldsymbol{X}}_{BC}^{t} + \Delta \boldsymbol{C}_s^t + (\mathbb{A}_{BC}^{t+\Delta t} + \mathbb{B}_{BC}^{t+\Delta t}\sigma_{BC}^t)\Delta t, \tag{4.11}$$

where $\mathbb{A}_{BC}^{t+\Delta t}$ and $\mathbb{B}_{BC}^{t+\Delta t}$ are obtained from $\boldsymbol{A}_s^{t+\Delta t}$ and $\boldsymbol{B}_s^{t+\Delta t}$, which are the outputs of the second model, $\bar{\boldsymbol{X}}_{BC}^{t}$ is the coordinates of landmark m of sample s at time t obtained from clinical dataset, and $\Delta \boldsymbol{C}_s^t$ is the change in the center of sample s from time t to time $t + \Delta t$, obtained from the results of the first neural network. By this

definition, this model's relative approximation error, δ_{BC}, is calculated as

$$\delta_{BC} = \frac{1}{\mathcal{H}.N_T.N_m} \sum_{s=1}^{N_T} \sum_{m=1}^{N_m} \left\| \boldsymbol{X}_{sm}^{t+\Delta t} - \bar{\boldsymbol{X}}_{sm}^{t+\Delta t} \right\|. \tag{4.12}$$

Bio-informed Mechanistic Neural Network ($FFNN_{BM}$): Similar to $FFNN_{BC}$, in the first step of this model, $FFNN_{CR}$ predicts the coordinates of the center point of the vertebra at time $t + \Delta t$, followed by computing the transition vector from the center point of the sample from time t to $t + \Delta t$. The neural network $FFNN_{BM}$ then predicts the set of growth model parameters as an output using a mechanistic loss function; see Fig. 4.7. The input vectors are $\boldsymbol{I}_s^t = [\bar{\boldsymbol{X}}_s^t, \boldsymbol{\alpha}_s^t, t, \Delta t, \bar{\boldsymbol{\sigma}}_s^t]$ with the same definitions for $\bar{\boldsymbol{X}}_s^t, \boldsymbol{\alpha}_s^t$, and $\bar{\boldsymbol{\sigma}}_s^t$. The output of $FFNN_{CR}$ is $\boldsymbol{O}_{CR,s}^t = [\boldsymbol{C}_s^{t+\Delta t}]$ which remains the same and the output vectors to the second step is $\boldsymbol{O}_s^t = [\boldsymbol{A}_s^{t+\Delta t}, \boldsymbol{B}_s^{t+\Delta t}]$, with $\boldsymbol{A}_s^{t+\Delta t}$ and $\boldsymbol{B}_s^{t+\Delta t}$ representing the parameters of the physical growth equation. The corresponding algorithm is explained in App. C.

Similar to the $FFNN_{BC}$, we define the predicted landmark m of sample s, for each m and s, as

$$\boldsymbol{X}_{BM}^{t+\Delta t} = \bar{\boldsymbol{X}}_{BM}^t + \Delta \boldsymbol{C}_s^t + (\mathbb{A}_{BM}^{t+\Delta t} + \mathbb{B}_{BM}^{t+\Delta t} \sigma_{BM}^t) \Delta t. \tag{4.13}$$

The definitions are identical to those stated in the $FFNN_{BC}$ formulation. The relative approximation error for $FFNN_{BM}$ model, represented by δ_{BM}, is calculated using

$$\delta_{BM} = \frac{1}{\mathcal{H}.N_T.N_m} \sum_{s=1}^{N_T} \sum_{m=1}^{N_m} \| \boldsymbol{X}_{BM}^{t+\Delta t} - \bar{\boldsymbol{X}}_{BM}^{t+\Delta t} \|^2. \tag{4.14}$$

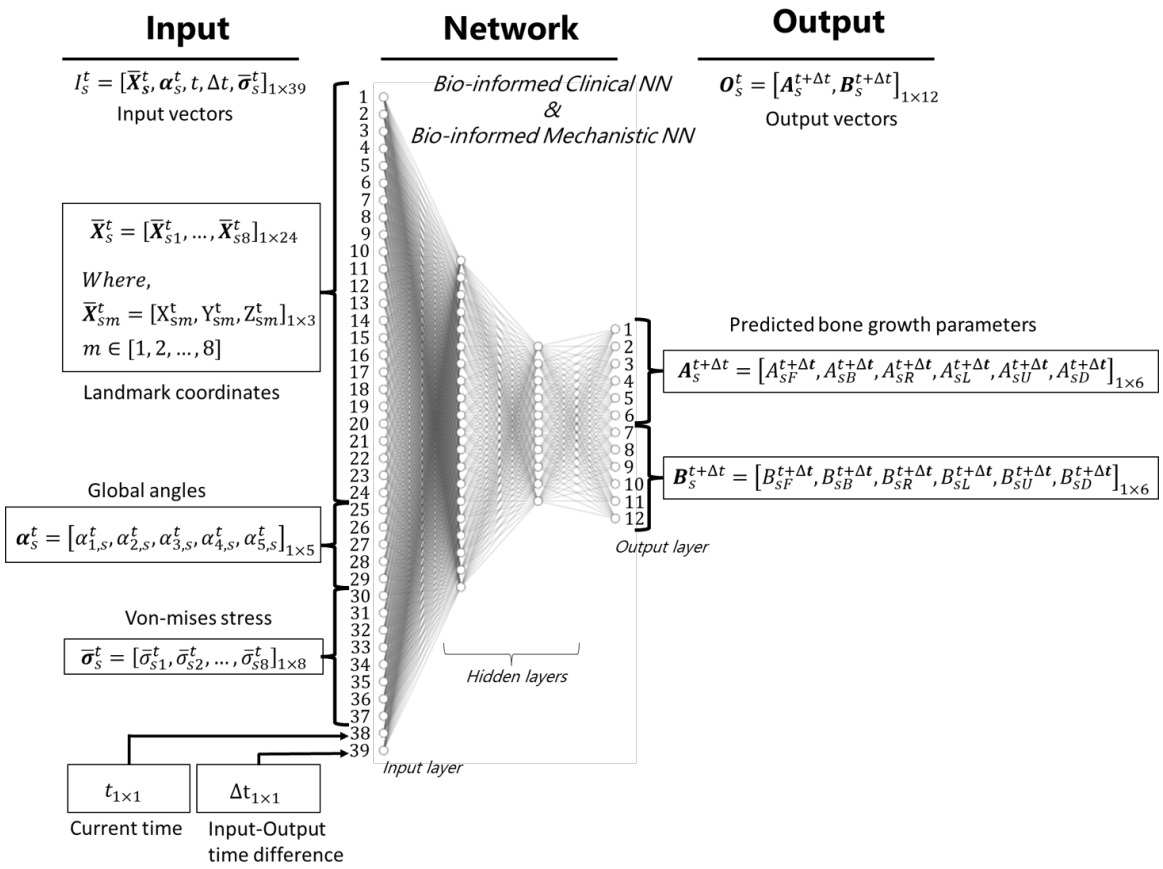

Figure 4.7. The architecture of a neural network for predicting the physical growth equation parameters. This structure is used in both $FFNN_{BC}$ and $FFNN_{BM}$ by defining two separate loss functions (one mechanistic and one non-mechanistic) [**1**].

4.4.4. Implementing the machine learning frameworks for prognosis spinal deformity

Data collection and feature selection: This part aims to provide a framework for prediction spinal deformity using the snake algorithm discussed in section 2. The database is comprised of clinical x-ray images. The snake algorithm is capable of

Table 4.3. Neural network setup for neural networks.

NN components	3D-Clinical	Bio-inf. Clinical		Bio-inf. Mechanistic	
	FFNN_{CL}	FFNN_{CR}	FFNN_{BC}	FFNN_{CR}	FFNN_{BM}
# training samples	68	68		68	
Size of training samples	31	39		39	
# test samples	51	51		51	
Size of test samples	24	3	12	3	12
# Hidden layers	2	2	2	2	2
Neurons in layer 1	20	20	20	20	20
Neurons in layer 2	10	10	10	10	10
Activation function	$ReLU$ function				

generating an infinite number of landmarks around each vertebra using x-ray images. Landmarks are classified into two types: those located on growth plates (X_G) and those that determine the vertebral sides (X_S), as illustrated in Fig. 4.1. The number of X_G landmarks on each 2D plane in this application is four, signifying the corner points that are expected to be on the growth plates. As a result, in the $3D$ framework presented ($X_G = 8$ and $X_S = 8$) as shown in Fig. 4.8. At $t_0 = 124$ months, the patient's first x-ray image is obtained. The next four x-ray images are obtained at $t = 139, 149, 156, 168$ months and used to train the neural network. The remaining three x-ray images, collected at $t = 160, 179, 187$ months, are utilized to compare with the neural network findings as shown in Table 4.4. Each x-ray image depicts the form of the patient's spine at a specific age. Based on the explained machine learning framework explained in section 4.4.2 the 3D-Clinical, Bio-informed Clinical and the Bio-informed Mechanistic NN are setup as explained in Table 4.3. It should be noted that the growth landmarks are tesed for each framework, and the relative approximation error indicated in Table 4.5 is determined for all landmarks, including

growth and side landmarks. The data is normalized before being fed to the model since the range and units of the input matrix are not the same.

Table 4.4. Data collection for the clinical, semi-mechanistic and mechanistic neural network.

Identification of x-ray images	Age (months)
Initial x-ray image	124
Output training x-ray images	$\{139, 149, 156, 168\}$
Output testing x-ray images	$\{160, 179, 187\}$

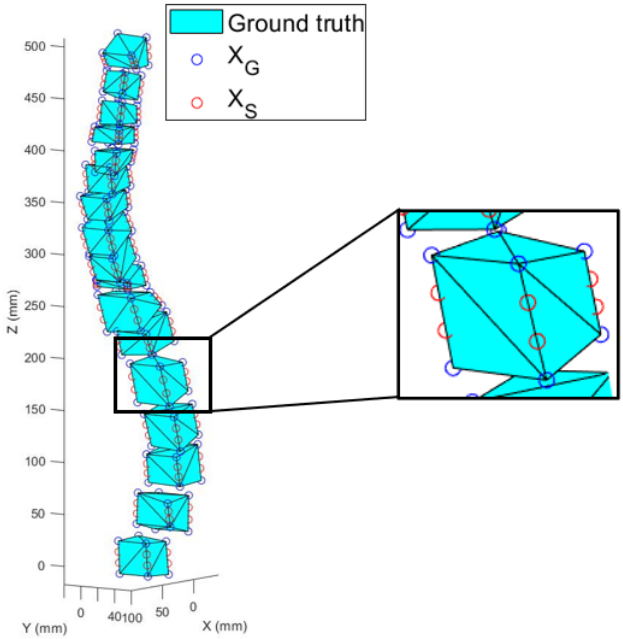

Figure 4.8. Illustration of the growth landmarks and side landmarks. There are 8 growth landmarks ($X_G = 8$) and 8 side landmarks($X_S = 8$) [**1**].

Results and cross validation on the data: The findings obtained from the patient described in Table 4.4 are presented here to illustrate the accuracy of the bio-informed mechanistic neural network prediction. The NN reconstruction process is the same as

that explained in section 4.4.2. A breakdown of the data used for training and testing can be seen in Table 4.4. Fig. 4.9 shows a comparison of the ground truth (actual data acquired from X-ray scans) and $FFNN_{CL}$ for the age of 160 months which is inside of the range of the training data and 179 and 187 for the outside of the range of the training data. The results are visualized for the eight corner points signifying the growth landmarks. Due to the 3D-Clinical NN's nature, the framework fails to forecast the ground truth. This framework is built on interpolation, and when it comes to the PS prediction, where the available data is insufficient, the model cannot learn from the available data, hence it fails to predict both inside and outside of the range. Fig. 4.10 shows the results for the $FFNN_{CR-BC}$ framework applied on the same dataset. $FFNN_{CR-BC}$ is the series architecture of $FFNN_{CR}$ and $FFNN_{BC}$ as explained in Appendix C. The results are $3D$ reconstructed based on the growth parameters obtained by $FFNN_{CR-BC}$ (Figs. 4.10 a,c and e) and the corresponding AP views are visualized in Figs. 4.10 b,d and f respectively. Because the findings are recreated using the bone growth model, this framework delivers a more accurate prediction than $FFNN_{CL}$. The data are next examined for the $FFNN_{CR-BM}$, as illustrated in Fig. 4.11. Similar to $FFNN_{CR-BC}$, $FFNN_{CR-BM}$ is the series architecture of $FFNN_{CR}$ and $FFNN_{BM}$ as explained in Appendix C. Due to the implementation of the mechanistic loss function, the results are the best when compared to the $FFNN_{CL}$ and $FFNN_{CR-BC}$ and are compatible with the ground truth obtained from X-ray images.

A cross validation study is carried out to see how the input and output data impact the framework error, as shown in Table 4.5. The term "cross validation" refers to

the process of determining how well a prediction model will work in practice [**87**]. We preserve the past two ages as test cases and rotate the test case inside the prior age span since we are more interested in prediction outside of the range. We can see from Table 4.5 that the prediction error of $FFNN_{CR-BM}$ is always lower than that of $FFNN_{CL}$ and $FFNN_{CR-BC}$, and that it can predict future spine curvature with a small error. The relative errors are calculated based on the Eqs. (4.10), (4.12) and (4.14) for $FFNN_{CL}$, $FFNN_{CR-BC}$ and $FFNN_{CR-BM}$ respectively. Table 4.6 refers to the cross validation on the $2D$ data using the existing Mechanistic framework [**6**] and $FFNN_{CR-BM}$. As it is shown, for each testing case, the present structure is more efficient. The suggested $FFNN_{CR-BM}$ enhances prediction accuracy by 40% for the inside of the range and 84.3% for the outside of the range.

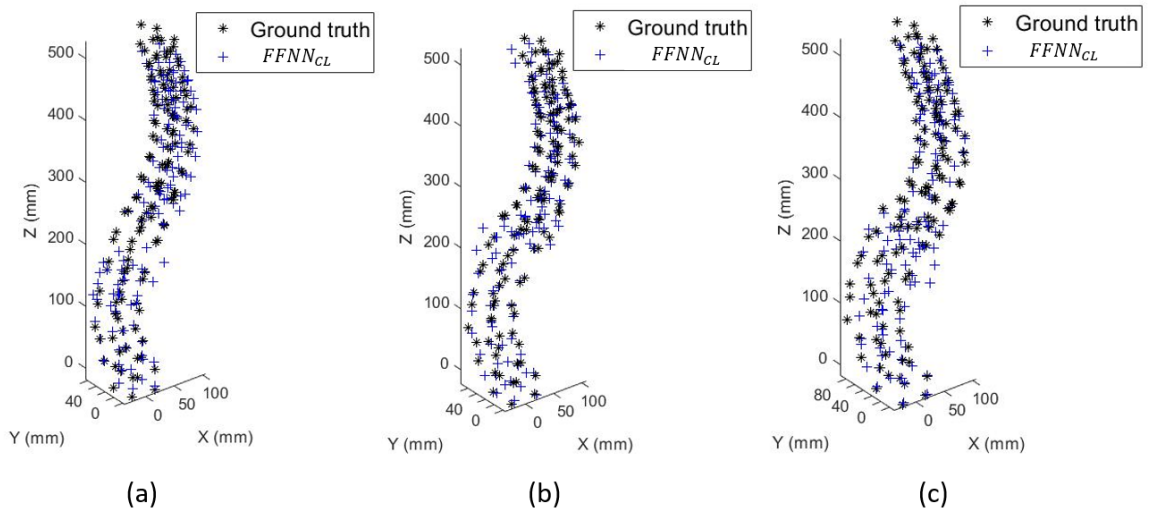

Figure 4.9. Differences between pure data science prediction ($FFNN_{CL}$) and ground truth (the results obtained by X-ray images) at age of (a) 160 Months (inside of the range of the trained data), (b) 179 Months (outside of the range of the trained data) and (c) 187 Months (outside of the range of the trained data). The landmarks are eight corner points of each vertebra. It is obvious that $FFNN_{CL}$ cannot predict the ground truth [**1**].

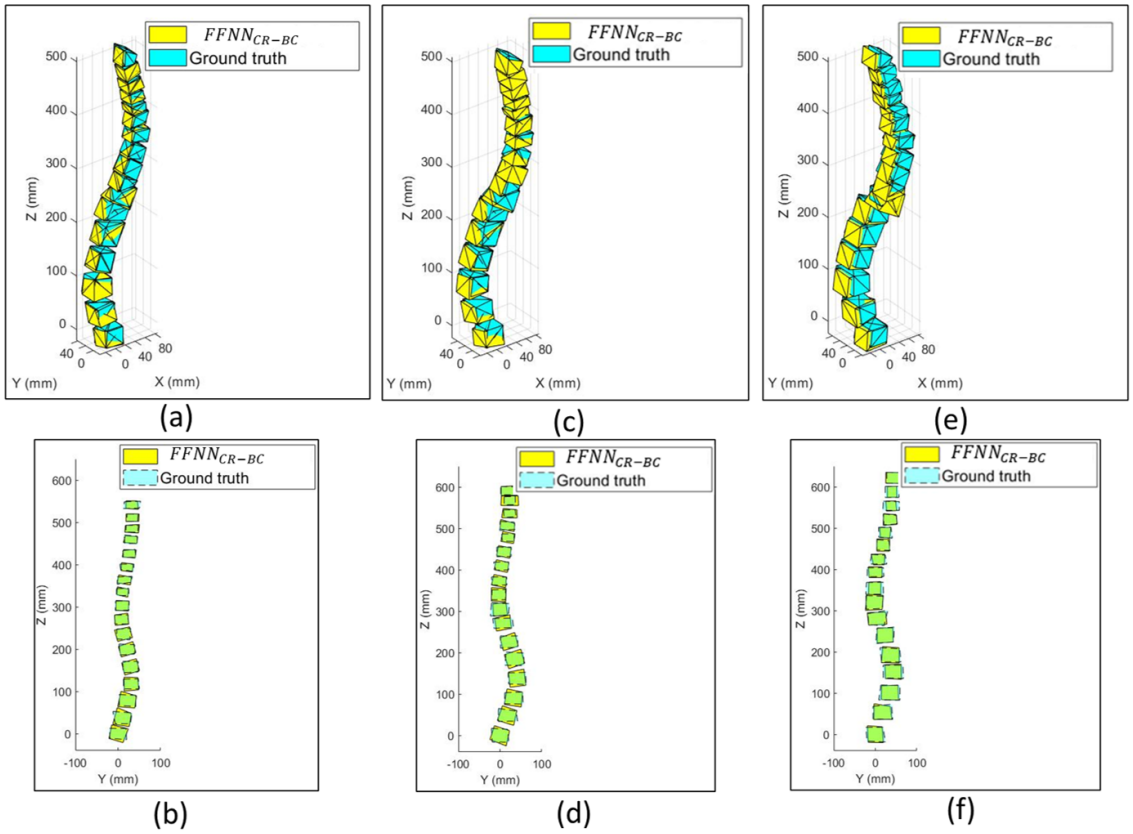

Figure 4.10. Differences between Bio-informed Clinical prediction ($FFNN_{CR-BC}$) and ground truth (the results obtained by X-ray images) at age of 160 Months (inside of the range of the trained data, a-b), 179 Months (outside of the range of the trained data, c-d), and 187 Months (outside of the range of the trained data, e-f). (a, c, e) show the 3D view and (b, d, f) show the 2D view on AP plane. The landmarks are eight corner points of each vertebra. It is obvious that $FFNN_{CR-BC}$ can predict the results close to ground truth [**1**].

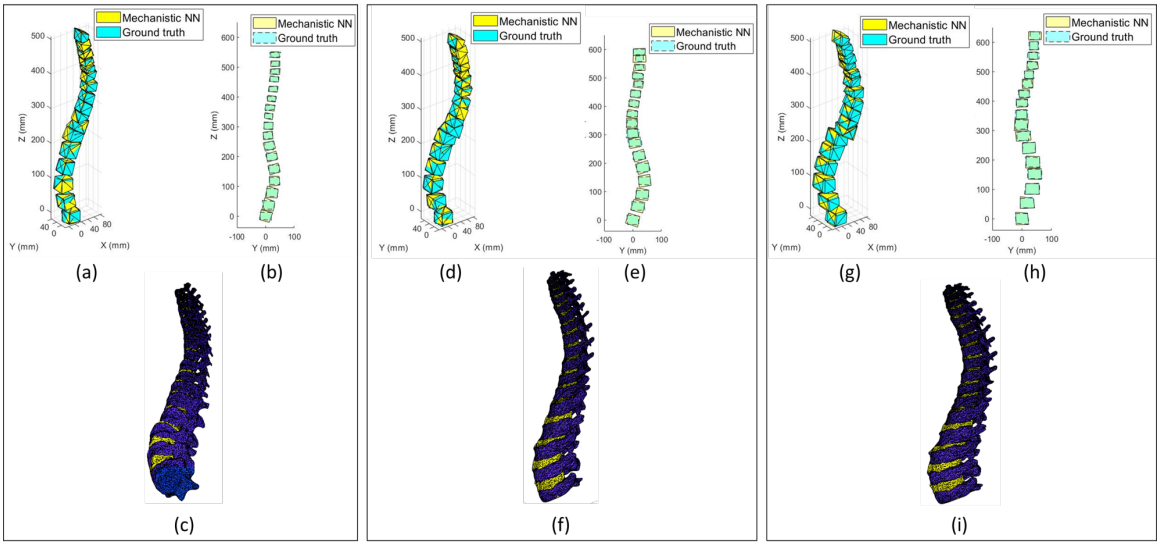

Figure 4.11. Differences between Bio-informed Mechanistic prediction ($FFNN_{CR-BM}$) and ground truth (the results obtained by X-ray images) at age of 160 Months (inside of the range of the trained data, a-c), 179 Months (outside of the range of the trained data, d-f) and 187 Months (outside of the range of the trained data, g-i). (a, d, g) show the 3D view, (b, e, h) show the 2D view on AP plane and (c, f, i) show the 3D reconstructed detailed geometry. The landmarks are eight corner points of each vertebra. $FFNN_{CR-BM}$ can clearly predict outputs that are close to ground truth [**1**].

Table 4.5. Cross validation study for three different neural networks. For each case, the testing data (blue cells) and training data (white cells) are shown. The relative approximation error is calculated for each prediction case [**1**].

Type of NN	Prediction performance						
	139	149	156	160	168	179*	187*
$FFNN_{CL}$	**2.74**					**1.68**	**2.72**
$FFNN_{CR-BC}$	**1.09**					**0.10**	**0.18**
$FFNN_{CR-BM}$	**0.68**					**0.02**	**0.04**
$FFNN_{CL}$		**0.94**				**0.31**	**0.23**
$FFNN_{CR-BC}$		**0.19**				**0.05**	**0.13**
$FFNN_{CR-BM}$		**0.10**				**0.02**	**0.03**
$FFNN_{CL}$			**0.4**			**0.20**	**0.23**
$FFNN_{CR-BC}$			**0.090**			**0.091**	**0.16**
$FFNN_{CR-BM}$			**0.08**			**0.02**	**0.032**
$FFNN_{CL}$				**0.25**		**0.11**	**0.45**
$FFNN_{CR-BC}$				**0.03**		**0.08**	**0.18**
$FFNN_{CR-BM}$				**0.01**		**0.02**	**0.03**
$FFNN_{CL}$					**0.14**	**0.23**	**1.18**
$FFNN_{CR-BC}$					**0.03**	**0.09**	**0.13**
$FFNN_{CR-BM}$					**0.015**	**0.018**	**0.02**

* Prediction at age outside of the range of trained data.

Table 4.6. Cross validation study for two different neural networks on 2D data for AP view (the mechanistic framework $FFNN_{ME}$ is borrowed from [**6**]). For each case, the testing data (blue cells) and training data (white cells) are shown. The relative approximation error is calculated for each prediction case. For each case, the Bio-informed Mechanistic approach has better performance [**1**].

Type of NN	Prediction performance						
	139	149	156	160	168	179*	187*
$FFNN_{CR-BM}$	**0.14**					**0.08**	**0.03**
$FFNN_{ME}$	**0.30**					**0.12**	**0.67**
$FFNN_{CR-BM}$		**0.05**				**0.07**	**0.02**
$FFNN_{ME}$		**0.07**				**0.3**	**0.53**
$FFNN_{CR-BM}$			**0.03**			**0.06**	**0.03**
$FFNN_{ME}$			**0.04**			**0.17**	**0.20**
$FFNN_{CR-BM}$				**0.04**		**0.08**	**0.03**
$FFNN_{ME}$				**0.08**		**0.24**	**0.32**
$FFNN_{CR-BM}$					**0.04**	**0.06**	**0.03**
$FFNN_{ME}$					**0.03**	**0.24**	**0.44**

* Prediction at age outside of the range of trained data.

CHAPTER 5

Conclusions and future works

5.1. Conclusions

The proposed work combines biomechanics, finite element analysis, advanced data science and image analysis technique to develop a predictive, patient-specific model for spine curvature in pediatric spinal deformity patients. Specifically, by taking advantage of the modified bone growth model, the iterative optimization of the deep learning framework consists of time-varying geometry-based parameters considered in the mechanistic loss function to minimize the error prediction while optimizing the dynamic parameters.

This research addresses the issues of limited data for validation of PSD model, variability of spinal growth among different patients and complexity of geometrical features of spines for predicting curvature. To develop the system, Lurie Hospital provided the anteroposterior and lateral views X-ray images of spine from PSD patients at different ages, treatment stages, and physical conditions. By adjusting geometric and fitting parameters in the active contour model, this study addressed one bottleneck of image segmentation. The segmented data are used to generate a 3D detailed model.

Patient-specific models of the spines are generated through image segmentation and surface registration methods with the help of clinical x-ray image data from Lurie

Hospital. These techniques can handle the complex geometry of vertebrae in human spine for 3D reconstructions. Thus, the proposed method has improved capability to capture progressive change in spine curvature for a specific patient compared to the existing models. It is a completely automated approach for detecting progressive change in spine curvature in detail for a single patient. A spine surrogate finite element model is generated along with the mesh generation. This framework incorporates time-dependent material models and time-dependent boundary conditions to reflect the effect of age and bone maturity in the surrogate model.

By merging medical data knowledge with a computational model, the presented framework addresses the problem of limited data for PS study. By incorporating a mechanistic learning and physical simulation model along with clinical data, we design a bio-informed mechanistic neural network that can predict the spinal curve progression with time for a specific patient. The novelty of the proposed method lies in its generality in predictive capability i.e. unlike the traditional neural networks, it can predict outside the range of conditions specified in the training data.

5.2. Suggested on future works

5.2.1. Further improvement on diagnosis and prognosis steps

In the future work, calibration of material properties and boundary conditions can be performed to study their effect on the prediction error along with improving the robustness of the surrogate model using the ample number of *in-vitro* and *in-vivo* results from experiments. To investigate the effect of each contributing factor on the prediction error of the bio-informed mechanistic framework, further sensitivity

analysis is required regarding the noise in the input data of the machine learning framework and the mesh size of the surrogate model. For each kind of spinal abnormality, separate reference models may be created (i.e. kyphosis and lordosis). As a result, the corresponding reference model can be chosen based on the deformity type, and landmark registration can be performed on them to provide patient-specific volumetric mesh. To address this procedure, for a given X-ray data, cross correlation can be performed between the input data and the reference data sets. One potential method to perform cross correlation between images would be dynamics time warping (DTW) [**88**]. By applying cross correlation, the most similar image to the input data will be find among the reference data set images and the landmarks corresponding to the correlated image will be implemented as the reference model of the ICP method. The detailed 3D geometry will be generated by deforming the most similar reference model.

The introduced framework contains PS dynamic parameters. These characteristics may be used in dynamic finite element analysis of various tissues at a smaller scale. The suggested framework can also be used for other image-based study including tumor progression and cardiovascular applications. The whole process is computationally helpful for early detection and treatment planning of spinal illnesses such as Lordosis and Kyphosis. Future research might look at the same framework over a larger dataset to construct a real-time, patient-specific, optimal treatment plan based on the first visit.

5.2.2. Further improvement on treatment step

The physicians require real-time prediction of curvature in spine of PSD patients to prescribe most suitable path of treatment. If braces are to be designed for treatments, the design must consider the change in the shape of PSD patient's spine over the period of treatment. Therefore, the brace designers also require a real-time predictive scheme for proper design. Our proposed methodology offers a predictive scheme while considering all the complex factors including geometry, material property, physical conditions, etc. For fast calculation a physics-based reduced order model can be developed into our computational framework. Moreover, the geometric update will also be performed based on unsupervised learning assisted clusters on vertebral growth plates. Thus, the model will be able to calculate and predict the shape of vertebrae very quickly and the physicians can visualize the progression of spine in real time.

The treatment forces can be designed along with the reduced order model to come up with the optimized treatment plan. One potential approach is shown in Fig. 5.1. Predicted results of the bio-informed mechanistic NN would be the input of the treatment phase. Meanwhile, desired 3D features for correcting spinal deformity are introduced to the system. The error between the desired output and the bio-informed mechanistic NN output will be calculate and the result will be passed to a feedback controller. This controller will design treatment forces as a function of time to reach the desires. One example of the potential controller that can be used would be proportional–integral–derivative controller (PID controller or three-term controller. The output would be treatment force based on time. This framework can be replaced by a NN once the system is trained based on the error and treatment force

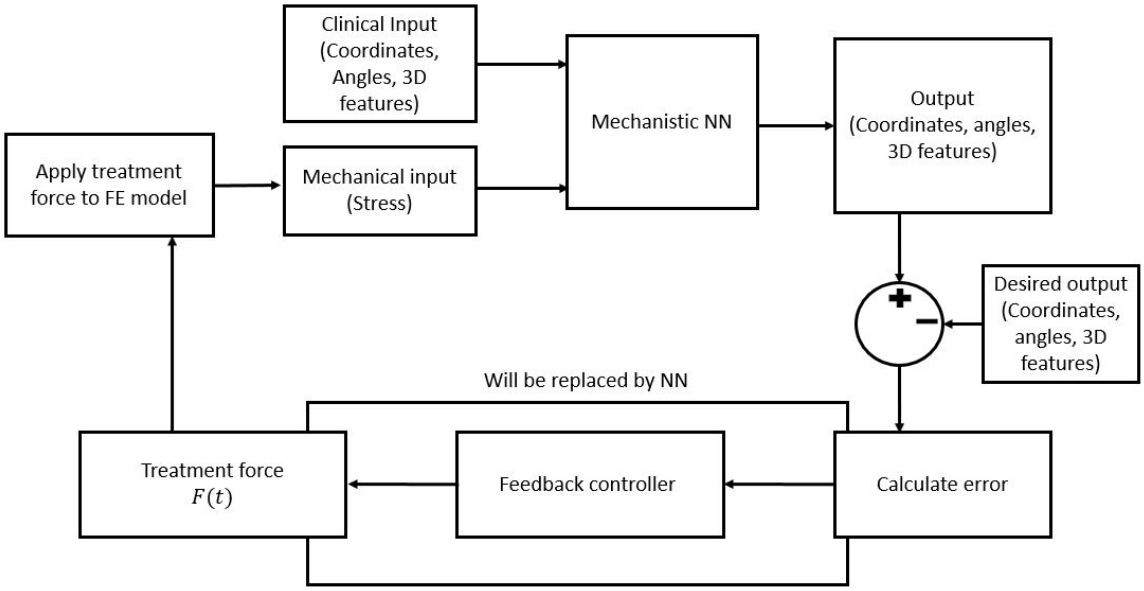

Figure 5.1. Future project plan. The clinical features will be extracted from X-ray data and mechanical data is obtained from the surrogate model. The predicted output will be compared to the desired one and the treatment force can be designed accordingly and pass it to the finite element model. The loop can be repeated until convergence.

as a function of time (the controller can be recruited as the supervisor of the NN). This treatment force will be applied to the FE model to get mechanistic data and the result will be passed to the Mechanistic NN. This loop will repeat until convergence.

References

[1] Mahsa Tajdari, Farzam Tajdari, Pouyan Shirzadian, Aishwarya Pawar, Sourav Saha, Toon Huysmans, Yu Song, Yongjie Jessica Zhang, John F. Sarwark, and Wing Kam Liu. Next generation prognosis framework for pediatric spinal deformities using bio-informed deep learning networks. *Submitted in special issue on "Image-based methods of computational medicines" of Engineering with Computers*, submitted Jan 31, 2022.

[2] Mahsa Tajdari, Aishwarya Pawar, Hengyang Li, Farzam Tajdari, Ayesha Maqsood, Emmett Cleary, Sourav Saha, Yongjie Jessica Zhang, John F Sarwark, and Wing Kam Liu. Image-based modelling for adolescent idiopathic scoliosis: Mechanistic machine learning analysis and prediction. *Computer methods in applied mechanics and engineering*, 374:113590, 2021.

[3] Hengyang Li, Orion L Kafka, Jiaying Gao, Cheng Yu, Yinghao Nie, Lei Zhang, Mahsa Tajdari, Shan Tang, Xu Guo, Gang Li, et al. Clustering discretization methods for generation of material performance databases in machine learning and design optimization. *Computational Mechanics*, 64(2):281–305, 2019.

[4] Adam R Meir, Jeremy CT Fairbank, Deborah A Jones, Donal S McNally, and Jill PG Urban. High pressures and asymmetrical stresses in the scoliotic disc in the absence of muscle loading. *Scoliosis*, 2(1):4, 2007.

[5] Katie Tinning and Jason Acworth. Make your best guess: an updated method for paediatric weight estimation in emergencies. *Emergency Medicine Australasia*, 19(6):528–534, 2007.

[6] Farzam Tajdari, Naeim Ebrahimi Toulkani, and Nima Zhilakzadeh. Intelligent optimal feed-back torque control of a 6dof surgical rotary robot. In *2020 11th Power Electronics, Drive Systems, and Technologies Conference (PEDSTC)*, pages 1–6. IEEE, 2020.

[7] Zaifeng Fan, Peter A Smith, Gerald F Harris, Frank Rauch, and Ruta Bajorunaite. Comparison of nanoindentation measurements between osteogenesis

imperfecta type iii and type iv and between different anatomic locations (femur/tibia versus iliac crest). *Connective Tissue Research*, 48(2):70–75, 2007.

[8] Catherine G Ambrose, Miriam Soto Martinez, Xiaohong Bi, Juanita Deaver, Cole Kuzawa, Lindsey Schwartz, Brian Dawson, Angela Bachim, Urszula Polak, Brendan Lee, et al. Mechanical properties of infant bone. *Bone*, 113:151–160, 2018.

[9] Zainab Altai, Marco Viceconti, Amaka C Offiah, and Xinshan Li. Investigating the mechanical response of paediatric bone under bending and torsion using finite element analysis. *Biomechanics and Modeling in Mechanobiology*, 17(4):1001–1009, 2018.

[10] Gregory C Wiggins, Christopher I Shaffrey, Mark F Abel, and Arnold H Menezes. Pediatric spinal deformities. *Neurosurgical Focus*, 14(1):1–14, 2003.

[11] Markus Rafael Konieczny, Hüsseyin Senyurt, and Rüdiger Krauspe. Epidemiology of adolescent idiopathic scoliosis. *Journal of children's orthopaedics*, 7(1):3–9, 2013.

[12] Steven Girdler, Brian Cho, Christopher M Mikhail, Zoe B Cheung, Noor Maza, and Samuel Kang-Wook Cho. Emerging techniques in diagnostic imaging for idiopathic scoliosis in children and adolescents: a review of the literature. *World neurosurgery*, 136:128–135, 2020.

[13] Dejan Knez, Imad S Nahle, Tomaž Vrtovec, Stefan Parent, and Samuel Kadoury. Computer-assisted pedicle screw trajectory planning using ct-inferred bone density: A demonstration against surgical outcomes. *Medical physics*, 46(8):3543–3554, 2019.

[14] Dominic Mischler, Markus Windolf, Boyko Gueorguiev, Stefaan Nijs, and Peter Varga. Computational optimisation of screw orientations for improved locking plate fixation of proximal humerus fractures. *Journal of Orthopaedic Translation*, 25:96–104, 2020.

[15] J Goerres, A Uneri, T De Silva, M Ketcha, S Reaungamornrat, M Jacobson, S Vogt, G Kleinszig, G Osgood, JP Wolinsky, et al. Spinal pedicle screw planning using deformable atlas registration. *Physics in Medicine & Biology*, 62(7):2871, 2017.

[16] Fabio Müller, Simon Roner, Florentin Liebmann, José M Spirig, Philipp Fürnstahl, and Mazda Farshad. Augmented reality navigation for spinal pedicle screw instrumentation using intraoperative 3d imaging. *The Spine Journal*, 20(4):621–628, 2020.

[17] Florentin Liebmann, Simon Roner, Marco von Atzigen, Florian Wanivenhaus, Caroline Neuhaus, José Spirig, Davide Scaramuzza, Reto Sutter, Jess Snedeker, Mazda Farshad, et al. Registration made easy–standalone orthopedic navigation with hololens. *arXiv preprint arXiv:2001.06209*, 2020.

[18] Nazli Sarkalkan, Harrie Weinans, and Amir A Zadpoor. Statistical shape and appearance models of bones. *Bone*, 60:129–140, 2014.

[19] Julius Quinn Campbell and Anthony J Petrella. An automated method for landmark identification and finite-element modeling of the lumbar spine. *IEEE Transactions on Biomedical Engineering*, 62(11):2709–2716, 2015.

[20] Yongjie Jessica Zhang. *Image-based geometric modeling and mesh generation*, volume 3. Springer Science & Business Media, 2012.

[21] Yongjie Zhang. Challenges and advances in image-based geometric modeling and mesh generation. In *Image-Based Geometric Modeling and Mesh Generation*, pages 1–10. Springer, 2013.

[22] Thomas Baum, Jan S Bauer, Tobias Klinder, Martin Dobritz, Ernst J Rummeny, Peter B Noël, and Cristian Lorenz. Automatic detection of osteoporotic vertebral fractures in routine thoracic and abdominal mdct. *European radiology*, 24(4):872–880, 2014.

[23] J Andrew, Murathoti DivyaVarshini, Prerna Barjo, and Irene Tigga. Spine magnetic resonance image segmentation using deep learning techniques. In *2020 6th International Conference on Advanced Computing and Communication Systems (ICACCS)*, pages 945–950. IEEE, 2020.

[24] Ruixuan Li, Kenan Niu, Di Wu, and Emmanuel Vander Poorten. A framework of real-time freehand ultrasound reconstruction based on deep learning for spine surgery. In *10 th Conference on New Technologies for Computer and Robot Assisted Surgery, Date: 2020/09/28-2020/09/30, Location: Barcelona, Spain*, 2020.

[25] Maziar Raissi, Paris Perdikaris, and George E Karniadakis. Physics-informed neural networks: A deep learning framework for solving forward and inverse

problems involving nonlinear partial differential equations. *Journal of Computational physics*, 378:686–707, 2019.

[26] MG Roberts, EMB Pacheco, R Mohankumar, TF Cootes, and JE Adams. Detection of vertebral fractures in dxa vfa images using statistical models of appearance and a semi-automatic segmentation. *Osteoporosis international*, 21(12):2037–2046, 2010.

[27] SM Masudur Rahman Al Arif, Michael Gundry, Karen Knapp, and Greg Slabaugh. Improving an active shape model with random classification forest for segmentation of cervical vertebrae. In *International Workshop on Computational Methods and Clinical Applications for Spine Imaging*, pages 3–15. Springer, 2016.

[28] Timothy F Cootes. Fully automatic localisation of vertebrae in ct images using random forest regression voting. In *Computational Methods and Clinical Applications for Spine Imaging: 4th International Workshop and Challenge, CSI 2016, Held in Conjunction with MICCAI 2016, Athens, Greece, October 17, 2016, Revised Selected Papers*, volume 10182, page 51. Springer, 2017.

[29] PA Bromiley, JE Adams, and TF Cootes. Localisation of vertebrae on dxa images using constrained local models with random forest regression voting. In *Recent Advances in Computational Methods and Clinical Applications for Spine Imaging*, pages 159–171. Springer, 2015.

[30] Martin G Roberts, Timothy F Cootes, and Judith E Adams. Automatic location of vertebrae on dxa images using random forest regression. In *International Conference on Medical Image Computing and Computer-Assisted Intervention*, pages 361–368. Springer, 2012.

[31] Timothy F Cootes, Christopher J Taylor, David H Cooper, and Jim Graham. Active shape models-their training and application. *Computer vision and image understanding*, 61(1):38–59, 1995.

[32] Hans Lamecker, Thomas H Wenckebach, and H-C Hege. Atlas-based 3d-shape reconstruction from x-ray images. In *18th International Conference on Pattern Recognition (ICPR'06)*, volume 1, pages 371–374. IEEE, 2006.

[33] Ted Julien Tchinde Fotsin, Carlos Vázquez, Thierry Cresson, and Jacques De Guise. Shape, pose and density statistical model for 3d reconstruction of articulated structures from x-ray images. In *2019 41st Annual International Conference of the IEEE Engineering in Medicine and Biology Society (EMBC)*, pages 2748–2751. IEEE, 2019.

[34] Moritz Ehlke, Heiko Ramm, Hans Lamecker, Hans-Christian Hege, and Stefan Zachow. Fast generation of virtual x-ray images for reconstruction of 3d anatomy. *IEEE transactions on visualization and computer graphics*, 19(12):2673–2682, 2013.

[35] Hangkee Kim, Kisuk Lee, Dongchun Lee, and Nakhoon Baek. 3d reconstruction of leg bones from x-ray images using cnn-based feature analysis. In *2019 International Conference on Information and Communication Technology Convergence (ICTC)*, pages 669–672. IEEE, 2019.

[36] Cornelius Johannes Frederik Reyneke, Marcel Lüthi, Valérie Burdin, Tania S Douglas, Thomas Vetter, and Tinashe EM Mutsvangwa. Review of 2-d/3-d reconstruction using statistical shape and intensity models and x-ray image synthesis: Toward a unified framework. *IEEE reviews in biomedical engineering*, 12:269–286, 2018.

[37] Sylvain Deschênes, Guy Charron, Gilles Beaudoin, Hubert Labelle, Josée Dubois, Marie-Claude Miron, and Stefan Parent. Diagnostic imaging of spinal deformities: reducing patients radiation dose with a new slot-scanning x-ray imager. *Spine*, 35(9):989–994, 2010.

[38] A Le Bras, S Laporte, D Mitton, JA De Guise, and W Skalli. Three-dimensional (3d) detailed reconstruction of human vertebrae from low-dose digital stereoradiography. *European Journal of Orthopaedic Surgery & Traumatology*, 13(2):57–62, 2003.

[39] Jean Dubousset, Georges Charpak, Irene Dorion, Wafa Skalli, Francois Lavaste, Jacques Deguise, Gabriel Kalifa, and Solene Ferey. A new 2d and 3d imaging approach to musculoskeletal physiology and pathology with low-dose radiation and the standing position: the eos system. *Bulletin de l'Academie nationale de medecine*, 189(2):287–97, 2005.

[40] Maxim Bashkuev, Sandra Reitmaier, and Hendrik Schmidt. Effect of disc degeneration on the mechanical behavior of the human lumbar spine: a probabilistic finite element study. *The Spine Journal*, 18(10):1910–1920, 2018.

[41] Maxim Bashkuev, Sandra Reitmaier, and Hendrik Schmidt. Relationship between intervertebral disc and facet joint degeneration: a probabilistic finite element model study. *Journal of biomechanics*, 102:109518, 2020.

[42] Mamadou T Bah, Prasanth B Nair, and Martin Browne. Mesh morphing for finite element analysis of implant positioning in cementless total hip replacements. *Medical engineering & physics*, 31(10):1235–1243, 2009.

[43] Angran Li, Amir Barati Farimani, and Yongjie Jessica Zhang. Deep learning of material transport in complex neurite networks. *Scientific reports*, 11(1):1–13, 2021.

[44] Michael M Moore, Einat Slonimsky, Aaron D Long, Raymond W Sze, and Ramesh S Iyer. Machine learning concepts, concerns and opportunities for a pediatric radiologist. *Pediatric radiology*, 49(4):509–516, 2019.

[45] Saba Pasha, Suken Shah, Peter Newton, Harms Study Group, et al. Machine learning predicts the 3d outcomes of adolescent idiopathic scoliosis surgery using patient–surgeon specific parameters. *Spine*, 46(9):579–587, 2021.

[46] Li Peng, Lan Lan, Peng Xiu, Guangming Zhang, Bowen Hu, Xi Yang, Yueming Song, Xiaoyan Yang, Yonghong Gu, Rui Yang, et al. Prediction of proximal junctional kyphosis after posterior scoliosis surgery with machine learning in the lenke 5 adolescent idiopathic scoliosis patient. *Frontiers in bioengineering and biotechnology*, 8, 2020.

[47] Ruixin Liang, Joanne Yip, Kai-Tsun Michael To, and Yunli Fan. Machine learning approaches to predict scoliosis. In *International Conference on Applied Human Factors and Ergonomics*, pages 116–121. Springer, 2021.

[48] Jae-sung Cho, Young-Shin Cho, Sang-Bok Moon, Mi-Jung Kim, Hyeok Dong Lee, Sung Young Lee, Young-Hoon Ji, Ye-Soo Park, Chang-Soo Han, and Seong-Ho Jang. Scoliosis screening through a machine learning based gait analysis test. *International Journal of Precision Engineering and Manufacturing*, 19(12):1861–1872, 2018.

[49] Sourav Saha, Zhengtao Gan, Lin Cheng, Jiaying Gao, Orion L Kafka, Xiaoyu Xie, Hengyang Li, Mahsa Tajdari, H Alicia Kim, and Wing Kam Liu. Hierarchical deep learning neural network (hidenn): An artificial intelligence (ai) framework for computational science and engineering. *Computer Methods in Applied Mechanics and Engineering*, 373:113452, 2021.

[50] Zhong He, Yimu Wang, Xiaodong Qin, Rui Yin, Yong Qiu, Kelei He, and Zezhang Zhu. Classification of neurofibromatosis-related dystrophic or nondystrophic scoliosis based on image features using bilateral cnn. *Medical Physics*, 48(4):1571–1583, 2021.

[51] Xiangbin Liu, Liping Song, Shuai Liu, and Yudong Zhang. A review of deep-learning-based medical image segmentation methods. *Sustainability*, 13(3):1224, 2021.

[52] Yongjie Jessica Zhang. *Geometric Modeling and Mesh Generation from Scanned Images*, volume 6. CRC Press, Taylor Francis Group, 2016.

[53] Fahad Lateef and Yassine Ruichek. Survey on semantic segmentation using deep learning techniques. *Neurocomputing*, 338:321–348, 2019.

[54] Fritz Hefti. *Pediatric Orthopedics in Practice*. Springer Science & Business Media, 2007.

[55] Y. J. Zhang. *Geometric Modeling and Mesh Generation from Scanned Images*. 2016.

[56] Michael Kass, Andrew Witkin, and Demetri Terzopoulos. Snakes: Active contour models‖ international journals of computer vision. 1988.

[57] Farzam Tajdari, Claudio Roncoli, and Markos Papageorgiou. Feedback-based ramp metering and lane-changing control with connected and automated vehicles. *IEEE Transactions on Intelligent Transportation Systems*, 2020.

[58] Henry R Cowell. Radiographic measurements and clinical decisions. *JBJS*, 72(3):319, 1990.

[59] JR Cobb. Outline for the study of scoliosis. *Instr Course Lect AAOS*, 5:261–275, 1948.

[60] CLIFFORD Gross, MICHAEL Gross, and STUART Kuschner. Error analysis of scoliosis curvature measurement. *Bulletin of the Hospital for Joint Diseases Orthopaedic Institute*, 43(2):171–177, 1983.

[61] Håkan Geijer, Bert Verdonck, Karl-Wilhelm Beckman, Torbjörn Andersson, and Jan Persliden. Digital radiography of scoliosis with a scanning method: radiation dose optimization. *European radiology*, 13(3):543–551, 2003.

[62] Hakan Geijer, Karl-Wilhelm Beckman, Berith Jonsson, Torbjorn Andersson, and Jan Persliden. Digital radiography of scoliosis with a scanning method: initial evaluation. *Radiology*, 218(2):402–410, 2001.

[63] DL Carman, RH Browne, and JG Birch. Measurement of scoliosis and kyphosis radiographs. intraobserver and interobserver variation. *The Journal of bone and joint surgery. American volume*, 72(3):328–333, 1990.

[64] Michaela Gstoettner, Katrin Sekyra, Nadja Walochnik, Peter Winter, Roland Wachter, and Christian M Bach. Inter-and intraobserver reliability assessment of the cobb angle: manual versus digital measurement tools. *European Spine Journal*, 16(10):1587–1592, 2007.

[65] Ricarda Lechner, David Putzer, Dietmar Dammerer, Michael Liebensteiner, Christian Bach, and Martin Thaler. Comparison of two-and three-dimensional measurement of the cobb angle in scoliosis. *International Orthopaedics*, 41(5):957–962, 2017.

[66] Matlab convhull function, 2020b. The MathWorks, Natick, MA, USA.

[67] Mehdi Khosrow-Pour. *Dictionary of information science and technology*, volume 1. IGI Global, 2006.

[68] Pramudita Satria Palar, Rhea Patricia Liem, Lavi Rizki Zuhal, and Koji Shimoyama. On the use of surrogate models in engineering design optimization and exploration: The key issues. In *Proceedings of the Genetic and Evolutionary Computation Conference Companion*, pages 1592–1602, 2019.

[69] M Dreischarf, T Zander, A Shirazi-Adl, CM Puttlitz, CJ Adam, CS Chen, VK Goel, A Kiapour, YH Kim, KM Labus, et al. Comparison of eight published static finite element models of the intact lumbar spine: predictive power of models improves when combined together. *Journal of biomechanics*, 47(8):1757–1766, 2014.

[70] Heath B Henninger, Shawn P Reese, Andrew E Anderson, and Jeffrey A Weiss. Validation of computational models in biomechanics. *Proceedings of the Institution of Mechanical Engineers, Part H: Journal of Engineering in Medicine*, 224(7):801–812, 2010.

[71] E Jolivet, E Daguet, V Pomero, D Bonneau, JD Laredo, and W Skalli. Volumic patient-specific reconstruction of muscular system based on a reduced dataset of medical images. *Computer methods in biomechanics and biomedical engineering*, 11(3):281–290, 2008.

[72] Aishwarya Pawar, Yongjie Zhang, Yue Jia, Xiaodong Wei, Timon Rabczuk, Chiu Ling Chan, and Cosmin Anitescu. Adaptive FEM-based nonrigid image

registration using truncated hierarchical B-splines. *Computers & Mathematics with Applications*, 72(8):2028–2040, 2016.

[73] Aishwarya Pawar, Yongjie Jessica Zhang, Cosmin Anitescu, Yue Jia, and Timon Rabczuk. Dthb3d_reg: dynamic truncated hierarchical b-spline based 3D nonrigid image registration. *Communications in Computational Physics*, 23(3), 2018.

[74] Aishwarya Pawar, Yongjie Jessica Zhang, Cosmin Anitescu, and Timon Rabczuk. Joint image segmentation and registration based on a dynamic level set approach using truncated hierarchical B-splines. *Computers & Mathematics with Applications*, 78:3250–3267, 2019.

[75] Lin Shi, Defeng Wang, Mark Driscoll, Isabelle Villemure, Winnie CW Chu, Jack CY Cheng, and Carl-Eric Aubin. Biomechanical analysis and modeling of different vertebral growth patterns in adolescent idiopathic scoliosis and healthy subjects. *Scoliosis*, 6(1):11, 2011.

[76] Huijie Leng, Michael J Reyes, Xuanliang N Dong, and Xiaodu Wang. Effect of age on mechanical properties of the collagen phase in different orientations of human cortical bone. *Bone*, 55(2):288–291, 2013.

[77] Albert Schultz, Gunnar Andersson, R Ortengren, K Haderspeck, and A Nachemson. Loads on the lumbar spine. validation of a biomechanical analysis by measurements of intradiscal pressures and myoelectric signals. *The Journal of Bone and Joint Surgery. American volume*, 64(5):713–720, 1982.

[78] Alf Nachemson. The load on lumbar disks in different positions of the body. *Clinical Orthopaedics and Related Research (1976-2007)*, 45:107–122, 1966.

[79] Antonius Rohlmann, Lars Bauer, Thomas Zander, Georg Bergmann, and Hans-Joachim Wilke. Determination of trunk muscle forces for flexion and extension by using a validated finite element model of the lumbar spine and measured in vivo data. *Journal of biomechanics*, 39(6):981–989, 2006.

[80] Brian Amberg, Sami Romdhani, and Thomas Vetter. Optimal step nonrigid icp algorithms for surface registration. In *2007 IEEE Conference on Computer Vision and Pattern Recognition*, pages 1–8. IEEE, 2007.

[81] Jiajun Zhang, Ka-yee Cheuk, Leilei Xu, Yujia Wang, Zhenhua Feng, Tony Sit, Ka-lo Cheng, Evguenia Nepotchatykh, Tsz-ping Lam, Zhen Liu, et al. A validated composite model to predict risk of curve progression in adolescent idiopathic scoliosis. *EClinicalMedicine*, 18:100236, 2020.

[82] Chen He, Michael Kai-Tsun To, Jason Pui-Yin Cheung, Kenneth Man-Chee Cheung, Chi-Kwan Chan, Wei-Wei Jiang, Guang-Quan Zhou, Kelly Ka-Lee Lai, Yong-Ping Zheng, and Man-Sang Wong. An effective assessment method of spinal flexibility to predict the initial in-orthosis correction on the patients with adolescent idiopathic scoliosis (ais). *PLoS One*, 12(12):e0190141, 2017.

[83] Jason Pui Yin Cheung, Prudence Wing Hang Cheung, Dino Samartzis, and Keith Dip-Kei Luk. Curve progression in adolescent idiopathic scoliosis does not match skeletal growth. *Clinical orthopaedics and related research*, 476(2):429, 2018.

[84] IAF Stokes. Mechanical effects on skeletal growth. *Journal of Musculoskeletal and Neuronal Interactions*, 2(3):277–280, 2002.

[85] Abien Fred Agarap. Deep learning using rectified linear units (relu). *arXiv preprint arXiv:1803.08375*, 2018.

[86] Matlab deep learning toolbox, 2018b. The MathWorks, Natick, MA, USA.

[87] Mervyn Stone. Cross-validatory choice and assessment of statistical predictions. *Journal of the Royal Statistical Society: Series B (Methodological)*, 36(2):111–133, 1974.

[88] Meinard Müller. Dynamic time warping. *Information retrieval for music and motion*, pages 69–84, 2007.

[89] Thorsten Guehring, Frank Unglaub, Helga Lorenz, Georg Omlor, Hans-Joachim Wilke, and Markus W Kroeber. Intradiscal pressure measurements in normal discs, compressed discs and compressed discs treated with axial posterior disc distraction: an experimental study on the rabbit lumbar spine model. *European Spine Journal*, 15(5):597–604, 2006.

[90] Katsuhiko Sato, Shinichi Kikuchi, and Takumi Yonezawa. In vivo intradiscal pressure measurement in healthy individuals and in patients with ongoing back problems. *Spine*, 24(23):2468, 1999.

APPENDIX A

Validation of the Surrogate Finite Element Model of Spine

The results of the generated finite element model are used to calculate the stress located on the top and bottom surfaces of each vertebra, which can provide a trend for prediction. The calculated stress will be used as an input for the mechanistic neural network for the prediction of curve progression. There are some methods to validate the results obtained by the spine finite element model. In this paper, the intervertebral disc (IVD) pressure is validated with the *in-vitro* results provided in [**89**].

One critical parameter to characterize spinal load and effect on the spine curve progression is IVD pressure. This parameter is among the few criteria that are directly controlled by the axial spinal load [**90**]. Maximum physiological IVD pressure is assumed to be between 0.1 MPa and 0.24 MPa [**89**]. However, scoliotic spine has higher pressure compared to the control patients. Figure A.1 demonstrates the von Mises stress distribution on IVD generated using ABAQUS software. As can be seen, the stress distribution is not symmetric on IVD (as it is expected) which leads to non-uniform growth of the vertebra and progression of scoliosis. The distribution of the von Mises stress can be compared with the experimental data provided in [**4**] in the intervertebral disc between L1-L2 vertebrae (Figure A.2). The stress is plotted along the path between concave and convex edges in the absence of muscle load. Since the experimental data is not taken from the same patient as the geometry in

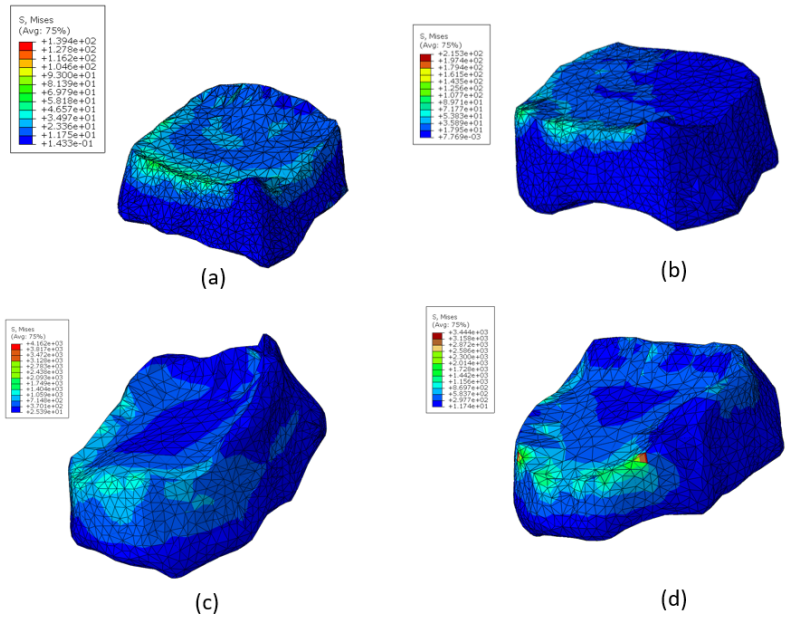

Figure A.1. Von Mises stress distribution on intervertebral disc between a) L3 and L4 vertebrae, b) L3 and L4 vertebrae, c) T1 and T2 vertebrae, and (d) T2 and T3 vertebrae ($10^2 Pa$) [**2**].

the finite element simulation, the maximum stress value is not the same. However, the distribution and range of the stresses are similar. The only purpose to visualize the comparison with the experimental data is demonstrating the not-symmetry trend of the stress distribution, and the magnitude of the stress should not be compared since the results are taken from different geometry with different material properties.

As mentioned earlier in chapter 3, the generated model is a surrogate model and we used the *indirect* validation method described in [**70**]. Indirect validation uses the experimental data that is not controlled by the user. This type of validation may seem unfavorable but it is unavoidable in this study since the *in-vivo* IVD stress distribution results of the distinct geometry is not available. Moreover, in this study the sensitivity analysis on the mesh size is not required in the surrogate model since

the results extracted from the surrogate model provides the trend of the output data used in the $FFNN_{BC}$ and $FFNN_{BM}$.

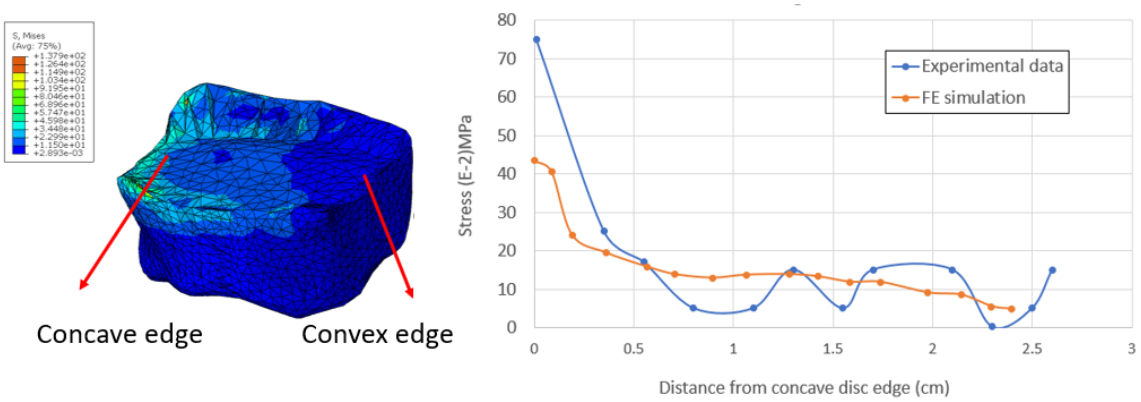

Figure A.2. Comparison of von Mises stress distribution of simulation and experimental data on disc L_{12} [**4, 2**].

Table A.1. Number of elements (N_E) and nodes (N_V) based on the optimally designed size of face triangle meshes in Appendix A, and the optimally designed mesh size (S) of the 3D finite element meshes of each vertebra and intervertebral disc (IVD).

Vertebra	N_E	N_V	$S(mm)$
L1	16,658	3,761	1.33
L2	16,168	3,685	1.19
L3	16,852	3,612	1.09
L4	16,165	3,687	1.24
L5	16,999	3,830	1.18
T1	22,845	4,762	1.07
T2	24,132	4,960	1.11
T3	22,631	4,762	1.18
T4	24,388	5,012	0.958
T5	24,221	5,005	0.956
T6	25,404	5,187	0.984
T7	25,808	5,255	0.953
T8	24,151	4,979	1.17
T9	22,475	4,729	0.954
T10	17,830	3,949	1.02
T11	17,549	3,919	1.15
T12	17,024	3,834	1.14

IVD	N_E	N_V	$S(mm)$
$L_{1,2}$	15,572	3,393	1.24
$L_{2,3}$	14,988	3,251	1.36
$L_{3,4}$	15,678	3,444	1.16
$L_{4,5}$	17,106	3,788	1.42
$T_{1,2}$	14,995	3,356	1.40
$T_{2,3}$	15,225	3,296	0.909
$T_{3,4}$	14,842	3,263	1.09
$T_{4,5}$	16,246	3,551	1.14
$T_{5,6}$	14,167	3,078	0.983
$T_{6,7}$	16,249	3,514	1.09
$T_{7,8}$	15,104	3,260	0.844
$T_{8,9}$	14,680	3,217	0.960
$T_{9,10}$	14,962	3,266	0.783
$T_{10,11}$	13,721	2,957	0.949
$T_{11,12}$	13,453	2,916	1.03
T_1L_5	18,257	3,726	0.950

Table A.2. Mechanical properties of cortical bone with time (data given as mean) for infant [**7, 8, 9**].

Age (months)	Elastic Modulus (MPa)
1	451.7
$(1, 2]$	645.8
$(2, 3]$	768.8
$(3, 4]$	768.8
$(4, 5]$	796.4
$(5, 6]$	886.1
$(6, 7]$	992.6
$(7, 8]$	1,980.3
$(8, 9]$	1,467.12
$(9, 10]$	1,417.9
$(10, 11]$	1,232.5
$(11, 24]$	1,848
$(24, 36]$	1,909
$(36, 48]$	1,883
$(48, 60]$	2,068
$(60, 72]$	2,155
$(72, 120]$	1,988
$(120, 158]$	1,995

APPENDIX B

Calculating growth parameters

Nodes with comparable growth behavior have the same growth parameters, as listed in Table 4.1. These parameters are considered to be the same for each vertebra. The first step in determining growth parameters for each vertebra v is to create growth equations for all nodes as presented in Eq. (4.3).

The equations are rewritten to represent the clustered label in each direction, using the same growth parameter assumption as mentioned before as

$$G^{tv}_{x_j} = \begin{cases} A^{tv}_{x_F} + B^{tv}_{x_F}\bar{\sigma}^{tv}_j & x^{tv}_j < 0, \\ A^{tv}_{x_B} + B^{tv}_{x_B}\bar{\sigma}^{tv}_j & x^{tv}_j \geq 0, \end{cases} \tag{B.1}$$

$$G^{tv}_{y_j} = \begin{cases} A^{tv}_{y_R} + B^{tv}_{y_R}\bar{\sigma}^{tv}_j & y^{tv}_j < 0, \\ A^{tv}_{y_L} + B^{tv}_{y_L}\bar{\sigma}^{tv}_j & y^{tv}_j \geq 0, \end{cases} \tag{B.2}$$

$$G^{tv}_{z_j} = \begin{cases} A^{tv}_{z_U} + B^{tv}_{z_U}\bar{\sigma}^{tv}_j & z^{tv}_j < 0, \\ A^{tv}_{z_D} + B^{tv}_{z_D}\bar{\sigma}^{tv}_j & z^{tv}_j \geq 0 \end{cases} \tag{B.3}$$

where x^{tv}_j, y^{tv}_j and z^{tv}_j are the coordinates in the local system of landmark j for the vertebra v at time t. The vectors A and B will be defined as

$$\begin{aligned} A &= [A_F, A_B, A_R, A_L, A_U, A_D], \\ B &= [B_F, B_B, B_R, B_L, B_U, B_D] \end{aligned} \tag{B.4}$$

to define the position dependent scalar value of growth parameters for each vertebra. To discretize the growth parameters in each direction, the vectors

$$\begin{cases} A_x = [A_F, A_F, A_F, A_F, A_B, A_B, A_B, A_B], \\ A_y = [A_R, A_L, A_R, A_L, A_R, A_L, A_R, A_L], \\ A_z = [A_U, A_U, A_D, A_D, A_U, A_U, A_D, A_D], \end{cases}$$

$$\begin{cases} B_x = [B_F, B_F, B_F, B_F, B_B, B_B, B_B, B_B], \\ B_y = [B_R, B_L, B_R, B_L, B_R, B_L, B_R, B_L], \\ B_z = [B_U, B_U, B_D, B_D, B_U, B_U, B_D, B_D], \end{cases} \tag{B.5}$$

are defined corresponding to the growth parameters in each direction for all the growth landmarks. In the presented frame work, the number of growth landmarks is $X_G = 8$, corresponding to 8 corner points shown in Fig. 4.2. To represent the matrix form of growth parameters for each vertebra, matrices $\mathbb{A}$ and $\mathbb{B}$ are developed as

$$\mathbb{A} = [A_x^T \;\; A_y^T \;\; A_z^T] \qquad \text{and} \qquad \mathbb{B} = [B_x^T \;\; B_y^T \;\; B_z^T]. \tag{B.6}$$

The dimension of $\mathbb{A}$ and $\mathbb{B}$ are 8×3 corresponding to 8 growth landmarks and 3 local coordinate directions (x, y and z). Calculating the growth parameters in each direction for all the 8 landmarks located on the growth plate can be obtained by

$$
\begin{bmatrix}
G_x^1 & G_y^1 & G_z^1 \\
G_x^2 & G_y^2 & G_z^2 \\
G_x^3 & G_y^3 & G_z^3 \\
G_x^4 & G_y^4 & G_z^4 \\
G_x^5 & G_y^5 & G_z^5 \\
G_x^6 & G_y^6 & G_z^6 \\
G_x^7 & G_y^7 & G_z^7 \\
G_x^8 & G_y^8 & G_z^8
\end{bmatrix}
=
\begin{bmatrix}
A_F & A_R & A_U \\
A_F & A_L & A_U \\
A_F & A_R & A_D \\
A_F & A_L & A_U \\
A_B & A_R & A_U \\
A_B & A_L & A_U \\
A_B & A_R & A_D \\
A_B & A_L & A_D
\end{bmatrix}
+
\begin{bmatrix}
B_F & B_R & B_U \\
B_F & B_L & B_U \\
B_F & B_R & B_D \\
B_F & B_L & B_U \\
B_B & B_R & B_U \\
B_B & B_L & B_U \\
B_B & B_R & B_D \\
B_B & B_L & B_D
\end{bmatrix}
\odot
\begin{bmatrix}
\bar{\sigma}_1 & \bar{\sigma}_1 & \bar{\sigma}_1 \\
\bar{\sigma}_2 & \bar{\sigma}_2 & \bar{\sigma}_2 \\
\bar{\sigma}_3 & \bar{\sigma}_3 & \bar{\sigma}_3 \\
\bar{\sigma}_4 & \bar{\sigma}_4 & \bar{\sigma}_4 \\
\bar{\sigma}_5 & \bar{\sigma}_5 & \bar{\sigma}_5 \\
\bar{\sigma}_6 & \bar{\sigma}_6 & \bar{\sigma}_6 \\
\bar{\sigma}_7 & \bar{\sigma}_7 & \bar{\sigma}_7 \\
\bar{\sigma}_8 & \bar{\sigma}_8 & \bar{\sigma}_8
\end{bmatrix}
\tag{B.7}
$$

where $\odot$ is the hadamard product.

APPENDIX C

Machine learning framework explanation

C.1. 3D-Clinical Neural Network ($FFNN_{CL}$):

The algorithm implemented for the $FFNN_{CL}$ is explained in the following equations.

3D-Clinical neural network (FFNN$_{\mathrm{CL}}$):

Input: $\boldsymbol{I}_s^t = [\bar{\boldsymbol{X}}_s^t, \boldsymbol{\alpha}_s^t, t_0, t]$.

Output: $\boldsymbol{O}_s^t = [\boldsymbol{X}_s^{t+\Delta t}]$.

Find $W_{ij}^l (l \in \{1,2,3\}), b_j^l (l \in \{2,3,4\})$ for each patient to minimize

$$loss_{CL}^t = \frac{1}{N_T}\frac{1}{N_m}\sum_{s=1}^{N_T}\sum_{m=1}^{N_m}\left\|\boldsymbol{X}_s^{t+\Delta t} - \bar{\boldsymbol{X}}_s^{t+\Delta t}\right\|^2, \tag{C.1}$$

where $\boldsymbol{O}_s^t = [\boldsymbol{X}_s^{t+\Delta t}] = \left[b_q^{l=4} + \sum_{k=1}^{N_N[l=3]} W_{qk}^{l=3} \mathscr{A}\left(a_{k,s}^{l=3}\right)\right]_{q=1}^{N_N[l=4]}$,

$a_{k,s}^{l=3} = b_k^{l=3} + \sum_{j=1}^{N_N[l=2]} W_{kj}^{l=2} \mathscr{A}\left(a_{j,s}^{l=2}\right)$,

$a_{j,s}^{l=2} = b_j^{l=2} + \sum_{i=1}^{N_N[l=1]} W_{ji}^{l=1} I_{i,s}^t$,

$\bar{\boldsymbol{X}}_s^{t+\Delta t}$ is from clinical dataset.

C.2. $FFNN_{CR-BC}$

The algorithm used for the $FFNN_{CR-BC}$ is explained in the following equations.

$FFNN_{CR-BC}$

Step 1 ($\mathrm{FFNN_{CR}}$*):*

Input: $\boldsymbol{I}_s^t = [\bar{\boldsymbol{X}}_s^t, \boldsymbol{\alpha}_s^t, t, \Delta t, \bar{\boldsymbol{\sigma}}_s^t]$.

Output: $\boldsymbol{O}_{CR,s}^t = [\boldsymbol{C}_s^{t+\Delta t}]$.

Find $W_{ij}^l (l \in \{1,2,3\}), b_j^l (l \in \{2,3,4\})$ for each patient to minimize

$$loss_{CR}^t = \frac{1}{N_T} \sum_{s=1}^{N_T} \left\| \boldsymbol{C}_s^{t+\Delta t} - \bar{\boldsymbol{C}}_s^{t+\Delta t} \right\|^2, \tag{C.2}$$

where $\boldsymbol{O}_{CR,s}^t = [\boldsymbol{C}_s^{t+\Delta t}] = \left[b_q^{l=4} + \sum_{k=1}^{N_N[l=3]} W_{qk}^{l=3} \mathscr{A}\left(a_{k,s}^{l=3}\right) \right]_{q=1}^{N_N[l=4]}$,

$a_{k,s}^{l=3} = b_k^{l=3} + \sum_{j=1}^{N_N[l=2]} W_{kj}^{l=2} \mathscr{A}\left(a_{j,s}^{l=2}\right)$,

$a_{j,s}^{l=2} = b_j^{l=2} + \sum_{i=1}^{N_N[l=1]} W_{ji}^{l=1} I_{i,s}^t$,

$\bar{\boldsymbol{C}}_s^{t+\Delta t}$ is from clinical dataset.

Step 2 ($\mathrm{FFNN_{BC}}$*):*

Input: $\boldsymbol{I}_s^t = [\bar{\boldsymbol{X}}_s^t, \boldsymbol{\alpha}_s^t, t, \Delta t, \bar{\boldsymbol{\sigma}}_s^t]$.

Output: $\boldsymbol{O}_s^t = [\boldsymbol{A}_s^{t+\Delta t}, \boldsymbol{B}_s^{t+\Delta t}]$

Find $W_{ij}^l (l \in \{1,2,3\}), b_j^l (l \in \{2,3,4\})$ for each patient to minimize

$$loss_{BC}^t = \frac{1}{N_T} \sum_{s=1}^{N_T} \left\| \boldsymbol{A}_s^{t+\Delta t} - \bar{\boldsymbol{A}}_s^{t+\Delta t} \right\|^2 + \left\| \boldsymbol{B}_s^{t+\Delta t} - \bar{\boldsymbol{B}}_s^{t+\Delta t} \right\|^2, \tag{C.3}$$

where $\boldsymbol{O}_s^t = [\boldsymbol{A}_s^{t+\Delta t}, \boldsymbol{B}_s^{t+\Delta t}] = \left[b_q^{l=4} + \sum_{k=1}^{N_N[l=3]} W_{qk}^{l=3} \mathscr{A}\left(a_{k,s}^{l=3}\right) \right]_{q=1}^{N_N[l=4]}$,

$a_{k,s}^{l=3} = b_k^{l=3} + \sum_{j=1}^{N_N[l=2]} W_{kj}^{l=2} \mathscr{A}\left(a_{j,s}^{l=2}\right)$,

$a_{j,s}^{l=2} = b_j^{l=2} + \sum_{i=1}^{N_N[l=1]} W_{ji}^{l=1} I_{i,s}^t$,

$\bar{\boldsymbol{A}}_s^{t+\Delta t}$ and $\bar{\boldsymbol{B}}_s^{t+\Delta t}$ are from clinical dataset.

C.3. $FFNN_{CR-BM}$

The algorithm implemented for the $FFNN_{CR-BM}$ is explained in the following equations.

$FFNN_{CR-BM}$

Step 1 ($\mathrm{FFNN_{CR}}$*):*

Input: $\boldsymbol{I}_s^t = [\bar{\boldsymbol{X}}_s^t, \boldsymbol{\alpha}_s^t, t, \Delta t, \bar{\boldsymbol{\sigma}}_s^t]$.

Output: $\boldsymbol{O}_{CR,s}^t = [\boldsymbol{C}_s^{t+\Delta t}]$.

Find $W_{ij}^l (l \in \{1,2,3\}), b_j^l (l \in \{2,3,4\})$ for each patient to minimize

$$loss_{CR}^t = \frac{1}{N_T} \sum_{s=1}^{N_T} \left\| \boldsymbol{C}_s^{t+\Delta t} - \bar{\boldsymbol{C}}_s^{t+\Delta t} \right\|^2, \tag{C.4}$$

where $\boldsymbol{O}_{CR,s}^t = [\boldsymbol{C}_s^{t+\Delta t}] = \left[b_q^{l=4} + \sum_{k=1}^{N_N[l=3]} W_{qk}^{l=3} \mathscr{A}\left(a_{k,s}^{l=3}\right) \right]_{q=1}^{N_N[l=4]}$,

$a_{k,s}^{l=3} = b_k^{l=3} + \sum_{j=1}^{N_N[l=2]} W_{kj}^{l=2} \mathscr{A}\left(a_{j,s}^{l=2}\right)$,

$a_{j,s}^{l=2} = b_j^{l=2} + \sum_{i=1}^{N_N[l=1]} W_{ji}^{l=1} I_{i,s}^t$,

$\bar{\boldsymbol{C}}_s^{t+\Delta t}$ is from clinical dataset.

Step 2 ($\mathrm{FFNN_{BM}}$*):*

Input: $\boldsymbol{I}_s^t = [\bar{\boldsymbol{X}}_s^t, \boldsymbol{\alpha}_s^t, t, \Delta t, \bar{\boldsymbol{\sigma}}_s^t]$.

Output: $\boldsymbol{O}_s^t = [\boldsymbol{A}_s^{t+\Delta t}, \boldsymbol{B}_s^{t+\Delta t}]$.

Find $W_{ij}^l (l \in \{1,2,3\}), b_j^l (l \in \{2,3,4\})$ for each patient to minimize

$$loss_{BM}^t = \frac{1}{N_T} \frac{1}{N_m} \sum_{s=1}^{N_T} \sum_{m=1}^{N_m} \|(\bar{\boldsymbol{X}}_{sm}^t + \Delta \bar{\boldsymbol{C}}_s^t + (\mathbb{A}_{sm}^{t+\Delta t} + \mathbb{B}_{sm}^{t+\Delta t} \sigma_{sm}^t)\Delta t) - \bar{\boldsymbol{X}}_{sm}^{t+\Delta t}\|^2, \tag{C.5}$$

where $\boldsymbol{O}_s^t = [\boldsymbol{A}_s^{t+\Delta t}, \boldsymbol{B}_s^{t+\Delta t}] = \left[b_q^{l=4} + \sum_{k=1}^{N_N[l=3]} W_{qk}^{l=3} \mathscr{A}\left(a_{k,s}^{l=3}\right) \right]_{q=1}^{N_N[l=4]}$,

$a_{k,s}^{l=3} = b_k^{l=3} + \sum_{j=1}^{N_N[l=2]} W_{kj}^{l=2} \mathscr{A}\left(a_{j,s}^{l=2}\right)$,

$a_{j,s}^{l=2} = b_j^{l=2} + \sum_{i=1}^{N_N[l=1]} W_{ji}^{l=1} I_{i,s}^t$,

$\mathbb{A}_{sm}^{t+\Delta t}$ and $\mathbb{B}_{sm}^{t+\Delta t}$ are obtained from $\boldsymbol{A}_s^{t+\Delta t}$ and $\boldsymbol{B}_s^{t+\Delta t}$, and

$\bar{\boldsymbol{X}}_{sm}^t, \bar{\boldsymbol{X}}_{sm}^{t+\Delta t}$, $\Delta \bar{\boldsymbol{C}}_s^t$ are from clinical dataset and σ_{sm}^t is from surrogate model.